Turbulence in a coastal environment: the case of Vindeby

Rieska Mawarni Putri[a], Etienne Cheynet[b], Charlotte Obhrai[a], and Jasna Bogunovic Jakobsen[a]

[a]Department of Mechanical and Structural Engineering and Materials Science, University of Stavanger, N-4036 Stavanger, Norway

[b]Bergen Offshore Wind Centre (BOW) and Geophysical Institute, University of Bergen, 5007 Bergen, Norway

Correspondence: Rieska Mawarni Putri (rieska.m.putri@uis.no)

Abstract. ~~Turbulence spectral characteristics for various atmospheric stratifications~~ The one-point and two-point power spectral densities of the wind velocity fluctuations are studied using the observations from an offshore mast at Vindeby ~~wind farm. Measurement data at 6 m, 18 m and 45 m above the~~ Wind Farm (Sea Mast West/SMW), for a wide range of thermal stratifications of the atmosphere. A comparison with predictions from the FINO1 platform (North Sea) is done to identify shared spectral characteristics of turbulence between different offshore sites. The sonic anemometer measurement data at 6, 18, and 45 m above mean sea level (amsl) are considered. ~~At the lowest height, the normalized power spectral densities of the velocity components show deviations from Monin-Obukhov similarity theory (MOST). A significant co-coherence at the wave spectral peak frequency between the vertical velocity component and the velocity of the sea surfaceis observed, but only when the significant wave heights exceed 0.9 m. The turbulence spectra at 18 m generally follow MOST and are consistent with the empirical spectra established~~ These heights are lower than at the FINO1 platform, where the measurements were collected at heights between 40 m and 80 m. Although the sonic anemometers are, to some extent, affected by transducer-flow distortion, the spectrum of the along-wind velocity component are consistent with those from FINO1 when surface-layer scaling is used and for near-neutral and moderately diabatic conditions ($z/L < 0.3$, where L is the Obukhov length and z is the height above the surface). For strongly stable or unstable conditions, deviations from the empirical spectral model fitted to the data recorded on the FINO1 ~~offshore platform from an earlier study. The data at 45 m is associated with a high-frequency measurement noise which limits its analysis to strong wind conditions only. The estimated~~ platform may be attributed to transducer-induced flow distortion and/or limited applicability of surface-layer scaling. The co-coherence of the along-wind component, estimated for vertical separations under near-neutral ~~atmosphere~~ conditions matches remarkably well with ~~those at~~ the predictions from FINO1. These findings mark an important step toward more comprehensive coherence models for wind load calculation. The turbulence characteristics estimated from the present dataset are valuable to better understand the structure of turbulence in the marine atmospheric boundary layer and are relevant for load estimations of offshore wind turbines. Yet, ~~a direct application of the results to other offshore or coastal sites should be exercised with caution, since the dataset is collected in shallow waters and at heights lower than the hub height of the current and the future~~ the data set recorded at Vindeby and FINO1 covers only the lower part of the rotor of state-of-the-art offshore wind turbines.

Therefore, further improvements in the characterisation of atmospheric turbulence for wind turbine design relies on measurements at heights above 100 m amsl.

1 Introduction

In the early 1990s, the first generations of offshore wind farms were commissioned to test the viability of extracting wind power in the marine atmospheric boundary layer (MABL). The first was ~~the Vindeby Wind farm~~ Vindeby Wind Farm which provided electricity to around 2,200 homes during its 25 years of operation, with a total generated power of 243 GWh (Power Technology, 2020). The project was deemed successful and marked the beginning of the offshore wind sector.

Not only was ~~the~~ Vindeby project the first offshore wind farm, but it also provided precious information on meteorological conditions in the MABL using offshore and onshore meteorological masts. The data collected has been used to study the characteristics of the mean wind speed profile under various atmospheric conditions (Barthelmie et al., 1994; Barthelmie, 1999). The masts were also instrumented with 3D sonic anemometers to study turbulence, but these data were used in a limited number of studies only (e.g. Mahrt et al., 1996, 2001).

The characteristics of the MABL differ from the overland atmospheric boundary layer (ABL) due to the larger proportion of the occurrence of non-neutral atmospheric stability conditions than on land (Barthelmie, 1999; Archer et al., 2016). Since the 2010s, several studies have indicated that diabatic wind conditions may significantly affect the fatigue life of offshore wind turbines (OWTs) components (Sathe et al., 2013; Hansen et al., 2014; Holtslag et al., 2016; Doubrawa et al., 2019; Nybø et al., 2020; Putri et al., 2020). Recent measurements from the first commercial floating wind farm (Hywind Scotland) have even shown the direct influence of the atmospheric stability on the floater motion (Jacobsen and Godvik, 2021). Diabatic conditions are more likely to affect floating wind turbines than bottom-fixed ones as the first few eigenfrequencies of large floating wind turbines are close to or below $0.20\,\mathrm{Hz}$ (Nielsen et al., 2006), which is the frequency range mainly affected by the thermal stratification of the atmosphere. To model properly the wind load for wind turbine designs, a better understanding of the spectral structure of turbulence in the MABL is necessary, which addresses partly the first of the three great challenges in the field of wind energy (Veers et al., 2019).

The limitations of current guidelines for offshore turbulence modelling, such as IEC 61400-1 (2005), have been highlighted in the past (Cheynet et al., 2017, 2018). Site-specific measurements advised by IEC 61400-1 (2005) are ~~justified for~~ related to the mean flow and integral turbulence characteristics. However, for the spectral characteristics, appropriate scaling can be used to display universal shapes over specific frequency ranges. In this regard, the present study addresses similar challenges as discussed by Kelly (2018) but focuses on some specific aspects not covered by the spectral tensor of homogeneous turbulence ~~, upon which the model by Kelly (2018) was developed: (1)~~ (Mann, 1994). Firstly, the low-frequency fluctuations are generally underestimated by the uniform-shear model, especially under convective conditions (De Maré and Mann, 2014; Chougule et al., 2018)~~and (2)~~. Secondly, the vertical coherence of turbulence is not always described accurately by the spectral tensor (Mann, 1994; Cheynet, 2019).

Using the unexplored sonic anemometer data from ~~the~~ Vindeby database, this study looks at the characteristics of offshore turbulence in the frequency space. The objective is to quantify the similarities between these characteristics and those identified on ~~the~~ FINO1 ~~platform~~ (Cheynet et al., 2018). Such a comparison is relevant to ~~establish~~ establishing new offshore wind turbulence models that can be used to improve the design of ~~the~~ future multi-megawatt offshore wind turbines. Whereas the measurement data from ~~the~~ FINO1 ~~platform~~ were obtained $40\,\mathrm{km}$ away from the shore, at heights between $40\,\mathrm{m}$ and $80\,\mathrm{m}$ above the mean sea level (amsl), those from the Vindeby database were collected only $3\,\mathrm{km}$ from the seaside and ~~altitudes~~ at heights between $6\,\mathrm{m}$ and $45\,\mathrm{m}$ amsl. Therefore, the two ~~datasets~~ data sets offer a complementary description of wind turbulence above the sea.

The present study is ~~organized~~ organised as follow: Section 2 describes the instrumentation and the site topography. Section 3 summarises the data processing, the assumptions, and the models used to study the spectral characteristics of turbulence. Section 4 presents the methodology used to assess the data quality and selection of stationary velocity data. Section 5 first evaluates the applicability of surface-layer scaling for the anemometer records at $6\,\mathrm{m}$ amsl. Then, the one-point velocity spectra and co-coherence estimates from Vindeby are compared with ~~the~~ predictions from semi-empirical models ~~from the~~ established on FINO1 ~~platform~~ (Cheynet et al., 2018) to assess the similarities ~~between both sites.~~ of the spectral characteristics between the two sites. Finally, the applicability of the Vindeby database for the design of an adequate turbulence model for offshore wind turbines is discussed in Section 5.1.

2 Instrumentation and site description

Vindeby Wind Farm operated in Denmark from 1991 to 2016 and was decommissioned in 2017. It was located ~~about~~ $1.5\,\mathrm{km}$ to $3\,\mathrm{km}$ from the northwestern coast of Lolland Island (fig. 1). Due to its location, Vindeby may be regarded as a coastal site instead of an offshore one. Vindeby has a flat topography with an average elevation under $11\,\mathrm{m}$ amsl, whereas the water depth around the wind farm ranges from $2\,\mathrm{m}$ to $5\,\mathrm{m}$ (Barthelmie et al., 1994). As pointed out by Johnson et al. (1998), the average significant wave height H_s at Vindeby is under $1\,\mathrm{m}$. The water depth increases from ~~ca.~~ around $3\,\mathrm{m}$ in the proximity of the wind farm up to ~~ca.~~ approximately $20\,\mathrm{m}$, away from the northern side of the wind farm.

The wind farm ~~comprised of~~ comprised 11 Bonus $450\,\mathrm{kW}$ turbines arranged in two rows with $300\,\mathrm{m}$ spacing along the $325°$-$145°$ line and three meteorological masts (fig. 2). The three masts were the Land Mast (LM), the Sea Mast South (SMS), and the Sea Mast West (SMW) where the two latter were placed offshore (fig. 2). Both SMS and SMW were installed in 1993 and decommissioned in 2001 and 1998, respectively. Measurements from LM and SMS were used by Barthelmie (1999) to assess the influence of the thermal stratification of the atmosphere on coastal wind climates. The present study considers only wind measurements from SMW due to the availability of the data.~~Information on the measurement from LM and SMS linked to the atmospheric stability conditions can be found in Barthelmie (1999).~~

~~The~~ SMW was a triangular lattice tower with a height of $48\,\mathrm{m}$ amsl as sketched in fig. 3. The booms on the SMW were mounted on both sides of the tower at $46°$ and $226°$ from the north and are referred to as the northern and southern boom, respectively. The booms' length ranged from $1.6\,\mathrm{m}$ to $4.0\,\mathrm{m}$ and their diameter was $50\,\mathrm{mm}$ (Barthelmie et al., 1994). Three F2360a GILL 3-axis ultrasonic anemometers (SAs) were mounted on the southern booms at ~~$45\,\mathrm{m}$, $18\,\mathrm{m}$ and $6\,\mathrm{m}$~~ 45, 18, and $6\,\mathrm{m}$ amsl and operated with a sampling rate of $20\,\mathrm{Hz}$. Two Risø P2021 resolver wind vanes with wind direction transmitters

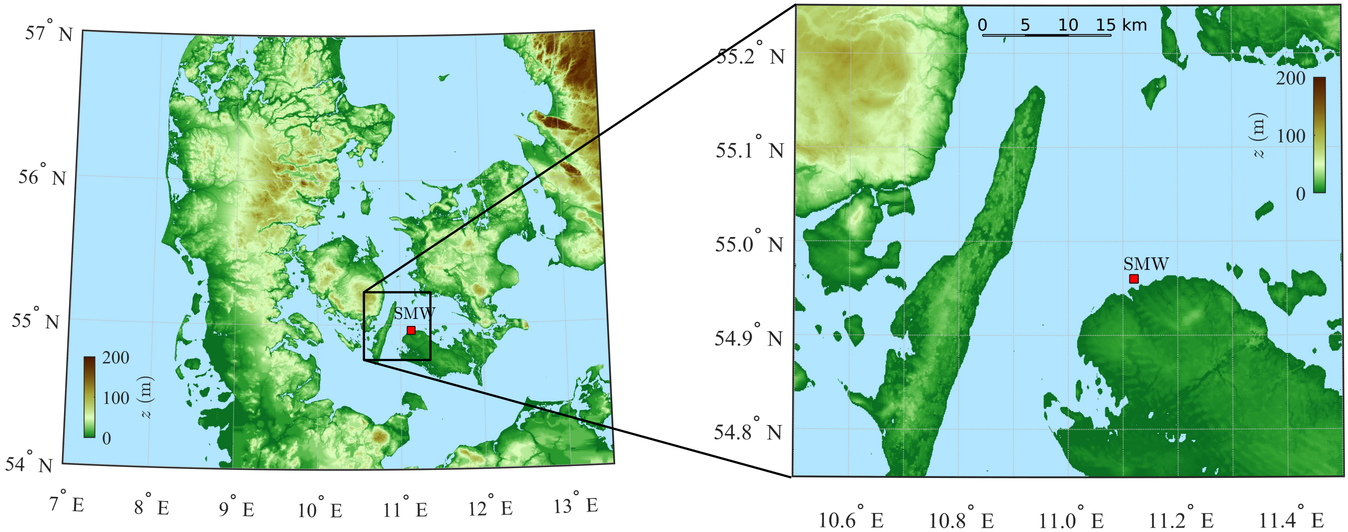

Figure 1. Digital elevation model of Southern Denmark showing the location of South Mast West (SMW), in a sheltered flat coastal environment.

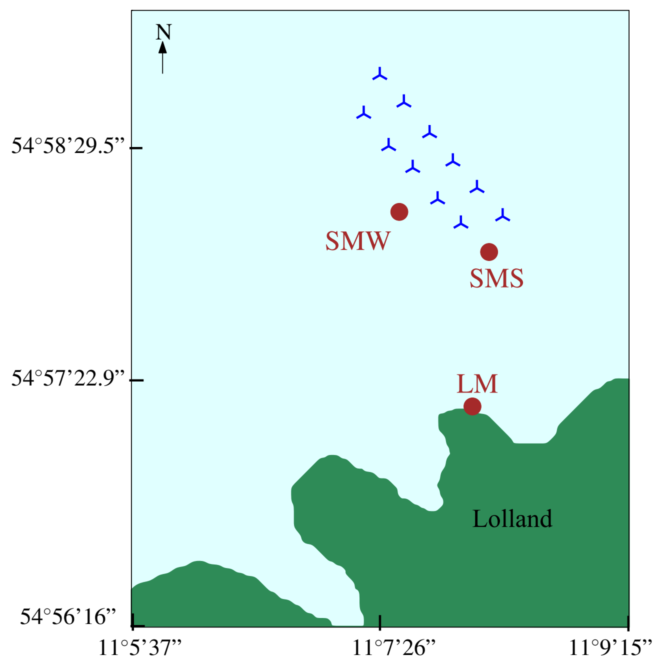

Figure 2. Vindeby Wind Farm layout with circles marking the position of the masts: SMW, SMS, and LM.

P2058 were located on the northern booms at 43 m and 20 m amsl using a sampling frequency of 5 Hz. The height of ~~the vanes and the cup anemometers'~~the vanes' centres above the boom was 600 mm. There were seven cup anemometers mounted on

SMW as shown in fig. 3. However, their measurements were not used here. The air temperature at $10\,\mathrm{m}$ amsl was recorded using a Risø P2039 PT 100 sensor. The sea surface elevation η was measured using an acoustic wave recorder (AWR) placed on the seabed, $30\,\mathrm{m}$ away from SMW, at a depth of $4\,\mathrm{m}$ (Johnson et al., 1998). The sea surface elevation data ~~was~~ were recorded at a sampling frequency of $8\,\mathrm{Hz}$ but stored with a sampling frequency of $20\,\mathrm{Hz}$.

The data collected from SMW were transferred to LM using an underwater fibre optic link and stored as time series of $30\,\mathrm{min}$ duration. Such a duration is appropriate to study ~~the wind turbulence~~turbulence at coastal and offshore areas (Dobson, 1981). Therefore, the flow characteristics studied herein are based on the averaging time of $30\,\mathrm{min}$.

The fetch around SMW ~~comprises of~~ comprises open sea, land, and mixed fetch as shown in fig. 1. The so-called sea fetch is considered when the wind blows from 220° to 90°, with a fetch distance up to $135\,\mathrm{km}$ for the sector ranging from 345° to 355°. The direction sectors from 0°-50° are those most affected by flow distortion due to the presence of the mast (Barthelmie et al., 1994). Furthermore, the flow from 335°-110° might be affected by the wake effects from the wind farm. To exclude the flow disturbed by the presence of the mast and ~~the wind turbines~~wind turbine wakes and/or internal boundary layers due to roughness changes, only the flow from 220°-330° is considered in the present study, which represents 40% of the velocity data recorded in 1994 and 1995 at SMW. The surface roughness ~~z_o~~ z_0 within 247° to 292° direction varies with the mean wind speed from $1.1 \times 10^{-4}\,\mathrm{m}$ to $1.2 \times 10^{-3}\,\mathrm{m}$ (Johnson et al., 1998). A more detailed description of the other directional sectors is given by Barthelmie et al. (1994).

3 Theoretical background

3.1 Monin-Obukhov theory

The along-wind, cross-wind, and vertical velocity components are denoted as u, v, and w, respectively. Each component is split into a mean ($\overline{u}$,$\overline{v}$,$\overline{w}$) and fluctuating part (u', v', w'). In flat and homogeneous ~~terrains~~terrain, the flow is fairly horizontal, i.e. $\overline{v}$ and $\overline{w}$ are approximatively zero. ~~To study turbulence for wind turbine design~~Here, the fluctuating components are assumed to be stationary, Gaussian, ergodic random processes (Monin, 1958).

Although the u-component drives the wind turbine's rotor fatigue loads, proper modelling of the v-component in terms of power spectral density (PSD) and root-coherence may be necessary for skewed flow conditions, which can occur because of a large wind direction shear (Sanchez Gomez and Lundquist, 2020) or wind turbine yaw error (Robertson et al., 2019). To estimate a wind turbine's fatigue loads, the vertical velocity component is likely more relevant in complex terrain than offshore (Mouzakis et al., 1999). Nevertheless, this component is studied here for the sake of completeness. Also, the vertical velocity component provides precious information on the sonic anemometer flow distortion (Cheynet et al., 2019; Peña et al., 2019). The vertical velocity component is also necessary to assess the atmospheric stability using the eddy covariance method and facilitates the study of the waves' influences on the velocity data recorded by the sonic anemometers (e.g. Benilov et al., 1974).

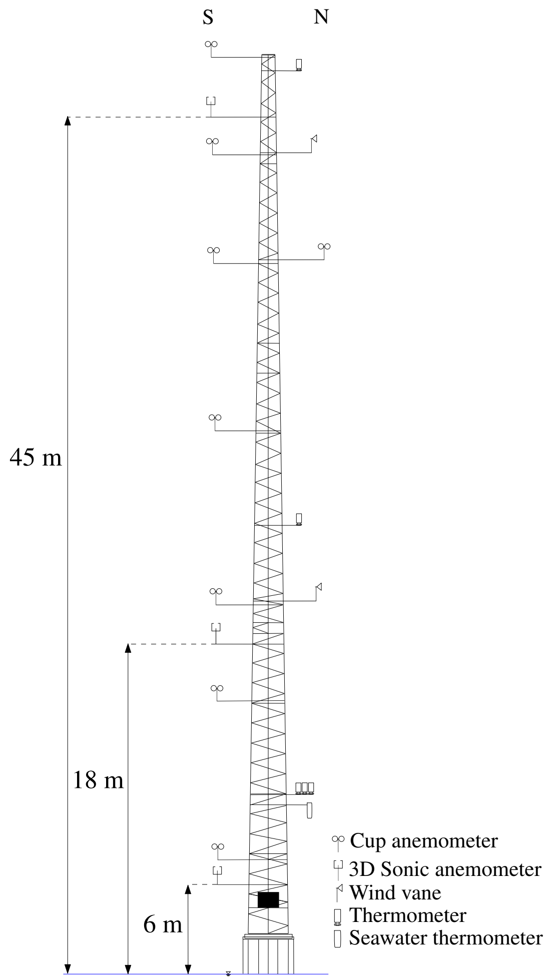

Figure 3. ~~Instrument arrangement~~ Sketch of the atmospheric instrumentation at SMW. The sonic anemometers are located in the southern boom 'S' oriented at 226° from the north.

In the atmospheric surface layer, where MOST generally applies, the scaling velocity is the friction velocity u_*, whereas the scaling lengths are the height z above the surface and the Obukhov length L (Monin and Obukhov, 1954), defined as

$$L = -\frac{u_*^3 \overline{\theta}_v}{g\kappa(\overline{w'\theta_v'})} \tag{1}$$

where $\overline{\theta}_v$ is the mean virtual potential temperature, $g = 9.81\,\mathrm{ms^{-2}}$ is the gravitational acceleration, $\kappa \approx 0.4$ is the von Kármán constant (Högström, 1985), and $\overline{w'\theta_v'}$ is the ~~flux~~ vertical flux of virtual potential temperature. For a given height z above the surface, the non-dimensional ~~Obukhov length~~ stability parameter $\zeta = z/L$ is used herein to classify the thermal stratification of the atmosphere.

While θ'_v can be fairly well approximated by the fluctuating sonic temperature measurement (Schotanus et al., 1983; Sempreviva and Gryning, 1996), the mean value $\overline{\theta}_v$ could not be reliably obtained from the sonic anemometers deployed on SMW (Kurt Hansen, private communication). Therefore, $\overline{\theta}_v$ was obtained using the absolute temperature recorded from ~~the~~ Risø P2039 PT 100 sensor at $10\,\mathrm{m}$ amsl, which was converted into the virtual potential temperature using the pressure data from LM and assuming an air relative humidity of 90% near ~~to~~ the sea surface (Stull, 1988). The air pressure data from LM is used due to the absence of air pressure data at SMW and SMS.

Because the covariance between the cross-wind and the vertical component may not be negligible in the MABL (Geernaert, 1988; Geernaert et al., 1993), the friction velocity u_* is computed as suggested by Weber (1999), that is

$$u_* = \sqrt[4]{\overline{u'w'}^2 + \overline{v'w'}^2} \tag{2}$$

A common approach to assess the applicability of MOST is to study the ~~ratio $\phi_w = \sigma_w/u_*$ and the~~ non-dimensional mean wind speed profile ϕ_m defined as

$$\phi_m\left(\frac{z}{L}\right) = \frac{\kappa z}{u_*}\frac{\partial \overline{u}}{\partial z} \tag{3}$$

as a function of the atmospheric stability (Kaimal and Finnigan, 1994). In the following, ~~ϕ_w and~~ ϕ_m ~~are empirically modelled such that following Kaimal and Finnigan (1994),~~ is empirically modelled as by Högström (1988),

$$\phi_m \approx \begin{cases} (1+15.2|\zeta|)^{-1/4}, & -2 \leq \zeta < 0 \\ 1+4.8(\zeta), & 0 \leq \zeta \leq 1 \end{cases} \quad \phi_w \approx \tag{4}$$

The validity of eq. (4) ~~and ??~~ is assessed for each anemometer in section 5.1. It should be noted that the presence of waves, especially swell, may invalidate MOST in the first few meters above the surface (Edson and Fairall, 1998; Sjöblom and Smedman, 2003b; Jiang, 2020) and this possibility will be discussed in section 5.2. Under convective conditions, the validity of MOST may also be questionable if the fetch is only a few kilometres long due to the presence of internal boundary layers (Jiang et al., 2020). In the present case, the choice of wind directions from 220° to 330° limits strongly the possibility that internal boundary layers are affecting the velocity measurements.

3.2 One-point turbulence spectrum

~~The~~ An appropriate modelling of the one-point velocity spectrum is ~~a key quantity to model the dynamic wind load~~ required to compute reliably the dynamic wind-induced response and the power production of wind turbines (Sheinman and Rosen, 1992; Hansen and Butterfield, 1993). ~~One-point integral~~ Integral turbulence characteristics, especially the turbulence intensity, are not always appropriate for turbulence characterisation (Wendell et al., 1991) which motivates the study of the spectral characteristics of turbulence ~~in the present study~~ herein.

Following Kaimal et al. (1972), the ~~normalized~~ normalised surface-layer one-point velocity spectra express a universal behaviour in the inertial subrange

$$\frac{fS_u(f)}{u_*^2\phi_\epsilon^{2/3}} \simeq 0.3 f_r^{-2/3} \text{ at } f_r \gg 1 \tag{5}$$

$$\frac{fS_v(f)}{u_*^2\phi_\epsilon^{2/3}} \approx \frac{fS_w(f)}{u_*^2\phi_\epsilon^{2/3}} \simeq 0.4 f_r^{-2/3} \text{ at } f_r \gg 1 \tag{6}$$

where $f_r = fz/\overline{u}$ and f is the frequency; S_u, S_v, and S_w are the velocity spectra for the along-wind, cross-wind, and vertical velocity component, respectively; ϕ_ϵ is the non-dimensional turbulent kinetic energy dissipation rate (Wyngaard and Coté, 1971):

$$\phi^{2/3}_{\epsilon} = \frac{\kappa z \epsilon}{u_*^3} \tag{7}$$

where ϵ is the turbulent kinetic energy dissipation rate~~, which is modelled herein as~~. In the present case, ϕ_ϵ is modelled as (Kaimal and Finnigan, 1994)

$$\phi_\epsilon^{2/3} = \begin{cases} 1 + 0.5|\zeta|^{2/3}, & \zeta \leq 0 \\ (1+5\zeta)^{2/3}, & \zeta \geq 0 \end{cases} \tag{8}$$

Equations (5) and (6) lead to the following relationships

$$\frac{S_v}{S_u} \approx \frac{S_w}{S_u} \simeq 1.33 \text{ at } f_r \gg 1 \tag{9}$$

Equation (9) is known as the assumption of local isotropy in the inertial subrange (Kolmogorov, 1941), although the latter may be reached without local isotropy (Mestayer, 1982; Chamecki and Dias, 2004). ~~Equations (5) and (6) are~~ Equation (9) provides convenient relationships not only to assess the data quality (Peña et al., 2019; Cheynet et al., 2019), but also to study the influence of waves on atmospheric turbulence, since a deviation from the $4/3$ law may be observed in the case of mixed-sea or swell (Smedman et al., 2003).

3.3 The coherence of turbulence

The coherence of turbulence describes the spatial correlation of eddies. The root-coherence is defined as the normalised cross-spectral density of turbulence and is a complex-valued function. The real part of the ~~coherence called~~ root-coherence known as the co-coherence, is one of the governing parameters for the structural design of wind turbines (IEC 61400-1, 2005). At vertical separations, the co-coherence $\cancel{\gamma_{ij}}\gamma_i$, where $i = \{u, v, w\}$, is defined as:

$$\gamma_i(z_1, z_2, f) = \frac{\mathrm{Re}\{S_i(z_1, z_2, f)\}}{\sqrt{S_i(z_1, f) S_i(z_2, f)}} \tag{10}$$

where $S_i(z_1, z_2, f)$ is the two-point cross-spectral density between heights z_1 and z_2, whereas $S_i(z_1, f)$ and $S_i(z_2, f)$ are the one-point spectra estimated at heights z_1 and z_2, respectively.

Davenport (1961) proposed an empirical model to describe the co-coherence for vertical separations, which depends only on a decay parameter c^i and a reduced frequency n:

$$\gamma_i(n) \approx \exp\left(\underline{c}-c^i n\right) \tag{11}$$

$$n = \frac{2 f d_z}{\overline{u}(z_1) + \overline{u}(z_2)} \tag{12}$$

where $d_z = |z_1 - z_2|$. For three heights $z_1 > z_2 > z_3$ such that $z_1 - z_2 = z_2 - z_3$, Davenport's model predicts that $\gamma_i(z_1, z_2, f)$ and $\gamma_i(z_2, z_3, f)$ collapse onto a single curve when expressed as a function of n. This ~~behavior~~behaviour, referred to as the Davenport's similarity herein, is questioned by Bowen et al. (1983) for vertical separations and by Kristensen et al. (1981) and Sacré and Delaunay (1992) for lateral separations.

Bowen et al. (1983) modified the Davenport model by assuming that c^i was a linear function of the distance, i.e.

$$c^i = c_1^i + \frac{2 c_2^i d_z}{(z_1 + z_2)} \tag{13}$$

Equation (13) reflects the blocking by the ground or the sea surface, which leads to an increase of the co-coherence with measurement height. This equation implies that the co-coherence decreases more slowly than predicted by the Davenport model if measurements are conducted far from the surface and at short separations. On the other hand, the co-coherence may decrease faster than predicted by the Davenport model if the measurements are associated with large separation distances. This implies that fitting the Davenport model to measurements with short or large separations may only lead to an inadequate design of wind turbines.

The model by Bowen et al. (1983) was further modified by Cheynet (2019) by including a third decay parameter c_3^i to account for the fact that the co-coherence cannot reach values of 1 at zero frequency ~~,~~unless the separation distance is zero. This led to the following three-parameter co-coherence functions, which is herein referred to as the modified Bowen model:

$$\gamma_{ii}(z_1, z_2, f) = \exp\left\{-\left[\frac{|z_2 - z_1|}{\overline{u}(z_1, z_2)}\sqrt{(c_1^i f)^2 + (c_3^i)^2}\right]\right\} \times \exp\left(-\frac{2 c_2^i f |z_2 - z_1|^2}{(z_1 + z_2)\,\overline{u}(z_1, z_2)}\right)$$

$$\gamma_{ii}(z_1, z_2, f) = \exp\left\{-\left[\frac{|z_2 - z_1|}{\overline{u}(z_1, z_2)}\sqrt{(c_1^i f)^2 + (c_3^i)^2}\right]\right\} \exp\left(-\frac{2 c_2^i f |z_2 - z_1|^2}{(z_1 + z_2)\,\overline{u}(z_1, z_2)}\right) \tag{14}$$

It should be noted that both c_1^i and c_2^i are dimensionless whereas c_3^i has the dimension of the inverse of a time. Following Kristensen and Jensen (1979), $c_3^i \propto 1/T$ where T is a time scale of turbulence. Therefore, low values of c_3^i are associated with a co-coherence converging toward 1 at low frequencies for which the separation distance is small compared to a typical turbulence length scale. The rotor diameter of multi-megawatt OWTs commissioned after 2015 in the North Sea is slightly larger than 150 m. For such structures, assuming $c_3^i \approx 0$ may no longer be appropriate.

IEC 61400-1 (2005) recommends the use of two empirical coherence formulations. The first one was derived based on the exponential coherence proposed by Davenport (1961), which read as

$$\gamma_u(f,d_z) = \exp\left\{-12\left[\sqrt{\left(\frac{f d_z}{\overline{u}_{hub}}\right)^2 + \left(0.12\frac{d_z}{8.1L_c}\right)^2}\right]\right\} \tag{15}$$

where $\overline{u}_{hub}$ is the mean wind speed at the hub height and

$$L_c = \begin{cases} 0.7z, & z \leq 60\,\mathrm{m} \\ 42\,\mathrm{m}, & z \geq 60\,\mathrm{m} \end{cases} \tag{16}$$

The second coherence model was derived based on a spectral tensor of homogeneous turbulence (Mann, 1994) but is not described in detail here. Further assessments of this model can be found in Mann (e.g. 1994), Saranyasoontorn et al. (2004) or Cheynet (2019).

4 Data processing

Sonic anemometer data monitored continuously from May 1994 to July 1995 were selected. No data ~~was~~ were collected in July 1994 and October 1994, leading to 13 months of available records. The sonic anemometer at $z = 18\,\mathrm{m}$ was chosen as the reference sensor throughout the data processing~~because the~~. The measurements at $z = 45\,\mathrm{m}$ were associated with a ~~low signal-to-noise ratio, which prevented a reliable estimation of the Obukhov length at this height. On the other hand,~~ higher measurement noise than at the ~~measurements at $z = 6\,\mathrm{m}$ were suspected to be located during a substantial amount of time in the wave boundary layer (WBL) (Sjöblom and Smedman, 2003a). This layer is also called as the wave sublayer by Emeis and Türk (2009), who suggest that its depth is approximately $5H_s$, although there is no consensus on the depth of the WBL. The WBL is defined hereinafter in a similar fashion as by Edson and Fairall (1998), i.e. it is the layer above the sea surface where $\phi_m(\zeta)$ or $\phi_w(\zeta)$ deviate from MOST. In this regard, the present definition differs slightly from Edson and Fairall (1998) or Sjöblom and Smedman (2003a) who did not study $\phi_w(\zeta)$ above the sea surface.~~other two heights. Although this noise was almost negligible at wind speed above $10\,\mathrm{m\,s^{-1}}$, it was visible in the velocity records at low wind speeds.

Since the wind sensors at 6, 18, and $45\,\mathrm{m}$ amsl were omnidirectional sonic anemometers, they were prone to flow distortion by the transducer. This flow distortion was investigated in terms of friction velocity estimated from the asymmetric solent anemometer mounted at $10\,\mathrm{m}$ amsl, between May 1994 and September 1994 only, due to data availability. The corrected friction velocities for the sensors at 6, 18, and $45\,\mathrm{m}$ were computed using the data at $10\,\mathrm{m}$, as elaborated in appendix B. When using the corrected friction velocity, no significant improvement was found for the ensemble-averaged normalised PSD estimates. It was then concluded that for the relatively narrow selected sector (220°-330°), the application of an ensemble averaging limits the influence of the transducer-induced flow distortion on the spectral flow characteristics. Therefore, it was decided not to apply a correction for both friction velocity and the Obukhov length to avoid over-processing the data.

Both the double rotation technique and the sectoral planar fit (PF) method (Wilczak et al., 2001) were considered to correct the tilt angles of the SAs. The choice of the algorithm relied on a comparison between the friction velocity u_* estimated using eq. (2) and the method by Klipp (2018), which does not require any tilt correction. The latter method provides an estimate u_{*R} of the friction velocity using the eigenvalues of the Reynolds stress tensor. Following this comparison, the double rotation technique was found to provide, in the present case, slightly more reliable results than the PF algorithm (see ~~??~~appendix A). It should be noted that this finding is likely specific to the Vindeby ~~dataset~~ data-set as the planar fit method usually provides better estimates of the ~~covariance of turbulence~~turbulent fluxes (Wilczak et al., 2001).

The time series were sometimes affected by ~~the outliers, which were removed~~ outliers. Here, the outliers were identified using a moving median window based on 5 min window length. The same outlier detection algorithm was also used for the sea surface elevation data, but with a moving window of 180 s. The local median values were then used to compute the median absolute deviation (MAD)~~(Leys et al., 2013)~~, as recommended by Leys et al. (2013). Data located more than five MAD away from the median were ~~classified as outliers and~~ replaced with NaNs. The ~~same outlier detection algorithm was also used for the sea surface elevation data, but with a moving window of 180 s.~~ generalised extreme Studentised deviate test (Rosner, 1983) was also assessed to detect outliers but did not bring significant improvements. When the number of NaNs in the time series was under 5%, they were replaced using a non-linear interpolation scheme based on the inpainting algorithm by D'Errico (2004) with the "spring" method. A more adequate but slower approach using autoregressive modelling (Akaike, 1969) was also applied but yielded a similar conclusion and therefore was not used. Time series containing more than 5% of NaNs were dismissed. Although other spike detection and interpolation algorithms exist in the literature (e.g. Hojstrup (1993)), the approach adopted in this study was found to provide an adequate trade-off between computation time and accuracy.

~~The moving average and a moving standard deviation with a window length of 10 min were used to~~ To assess the first- and second-order stationarity of the velocity ~~data, respectively.~~recordings, the moving mean and the moving standard deviation of the along-wind component were calculated using a window length of 10 min. The time series were considered as stationary when the two following criteria were fulfilled: (1) the maximum absolute relative difference between the moving mean and the static mean was lower than a threshold value of 20%; (2) for the moving standard deviation, the maximum absolute relative difference was also used with a threshold value of 40%. The choice of a larger threshold value for the moving standard deviation test is justified by the larger statistical uncertainty associated with the variance of a random process compared to its mean (Lumley and Panofsky, 1964).

Velocity records with an absolute value of skewness larger than 2 or a kurtosis below 1 or above 8 are likely to display an unphysical behaviour ~~due to e.g. high measurement noise~~ (Vickers and Mahrt, 1997) and were subsequently dismissed. The

Table 1. Percentage of the records between April 1994 to July 1995 from SMW that failed the quality-data assessment.

	6 m	18 m	45 m
NaNs > 5%	5%	< 1%	22%
Unphysical kurtosis and skewness	4%	3%	< 1%
Non-stationary	9%	15%	19%
Large statistical uncertainties	2%	4%	22%

statistical uncertainties of the records were quantified as by Wyngaard (1973) and Stiperski and Rotach (2016):

$$a_{ii}^2 = \frac{4z}{T\overline{u}}\left[\frac{\overline{i'^4}}{\sigma_i^4} - 1\right] \tag{17}$$

$$a_{uw}^2 = \frac{z}{T\overline{u}}\left[\frac{\overline{(u'w')^2}}{u_*^4} - 1\right] \tag{18}$$

$$a_{vw}^2 = \frac{z}{T\overline{u}}\left[\frac{\overline{(v'w')^2}}{u_*^4} - 1\right] \tag{19}$$

where a_{ij} with $i,j = (u,v,w)$ is the uncertainty associated with the variance and covariance estimates. Time series with a large random error, i.e. $a_{ii} > 0.20$ or $a_{ij} > 0.50$, $i \neq j$, were excluded.

The records with a mean wind speed below $5.0\,\mathrm{m\,s^{-1}}$ at $18\,\mathrm{m}$ amsl were discarded. Assuming a logarithmic mean wind profile, a near-neutral atmosphere, and a roughness length $z_0 = 2\times10^{-4}\,\mathrm{m}$ (WMO, 1983), the corresponding mean wind speed at ~~18 m amsl~~a typical offshore wind turbine hub height ($90\,\mathrm{m}$ amsl) is $5.7\,\mathrm{m\,s^{-1}}$. The present choice of a lower threshold mean wind speed is, therefore, consistent with the cut-in wind speed of large offshore wind turbines, which is $5.0\,\mathrm{m\,s^{-1}}$ at hub height. It ensures also a consistent comparison of the spectral characteristics of turbulence with the data collected at FINO1, where the lowest mean wind speed considered was $5.0\,\mathrm{m\,s^{-1}}$ at $80\,\mathrm{m}$ amsl.

The ~~power spectral density (PSD)~~ PSD estimates of the velocity fluctuations were evaluated using Welch's method (Welch, 1967) with a Hamming window, three segments, and 50% overlap. The spectra were ensemble-averaged using the median of multiple $30\,\mathrm{min}$ time series that passed the data-quality tests described above and were smoothed by using ~~a~~ bin-averaging over logarithmically-spaced bins. The co-coherence estimates were also computed using Welch's method but using eight segments and 50% overlap to further reduce the statistical uncertainty.

Table 1 displays the percentage of samples at each measurement height that failed the data-quality assessment. It relies on initial data availability of 86%, 97%, and 86% for the anemometers at ~~6 m amsl, 18 m amsl~~6, 18, and $45\,\mathrm{m}$ amsl, respectively. Following the criteria used in the data processing and Table 1, the percentage of data considered for the analysis was 69%, 76%, 45% at ~~6 m, 18 m and 45 m~~6, 18, and $45\,\mathrm{m}$ amsl, respectively. These percentages correspond to 1566 time series of $30\,\mathrm{min}$ duration for the SA at $6\,\mathrm{m}$, 1771 time series at $18\,\mathrm{m}$, and 854 at $45\,\mathrm{m}$. The data from SA at $45\,\mathrm{m}$ ~~shows~~ showed the highest portion of non-stationary and large statistical uncertainties compared to the other SAs. Furthermore, the SA at $45\,\mathrm{m}$ also contained the highest fraction of ~~NaN~~ NaNs in the time series, ~~which testified~~ due to a large number of outliers. The larger fraction of data ~~removed~~ removal for the anemometer at $45\,\mathrm{m}$ is attributed to the observed uncorrelated white noises in the signal. This measurement noise, which may be linked to the length of the cable joining the anemometer and the acquisition system, is usually small for wind speed above $10\,\mathrm{m\,s^{-1}}$. Therefore, it was decided not to filter it out using digital low-pass filtering techniques. Time series that were flagged as non-physical made up ~~only $< 5\%$~~ less than 5% for each SA in the present ~~datasets~~data set, likely because the test was applied after the outlier detection algorithm. The portion of non-stationary time series increased with height (see Table 1). Closer to the surface, the eddies are smaller and are less likely to be affected by the sub-meso or mesospheric atmospheric motion, which contribute to non-stationary fluctuations (Högström et al., 2002).

5 Results

5.1 Applicability of MOST

In the atmospheric surface layer, the friction velocity u_* is often assumed constant with the height (constant flux layer). However, fig. 4 shows that the friction velocity is generally larger at $6\,\mathrm{m}$ than at the other two measurement heights, especially under stable conditions. ~~The larger value of u_* at $6\,\mathrm{m}$ amsl than at $18\,\mathrm{m}$ amsl may reflect~~ The different friction velocity values at $6\,\mathrm{m}$ compared to $18\,\mathrm{m}$ and $45\,\mathrm{m}$ were suspected to be due to the transducer-induced flow distortion and/or the contribution of the wave-induced stress to the total turbulent stress ~~in the few meters above the sea surface (Janssen, 1989; Tamura et al., 2018)~~ (Janssen, 1989; Tamura et al., 2018).

The applicability of MOST is assessed by studying ~~ϕ_w and~~ ϕ_m as a function of ζ. ~~Each sub-panel of **??** shows ϕ_w at a different measurement height, whereas the black solid line corresponds to **??**. Under near-neutral conditions ($|\zeta| \leq 0.1$), $\phi_w \approx 1.32$ at $45\,\mathrm{m}$ amsl, $\phi_w \approx 1.24$ at $18\,\mathrm{m}$ amsl, and $\phi_w \approx 1.17$ at $6\,\mathrm{m}$ amsl. In flat and uniform terrains, a ratio of $\phi_w \approx 1.25$ is generally found for near-neutral conditions (Panofsky and Dutton, 1984, Table 7.1). The error bars associated with the estimates at $45\,\mathrm{m}$ are likely related to the presence of the uncorrelated white noises in the velocity records (Kaimal and Finnigan, 1994, section 7.4.2), which leads to an underestimation of u_*. The wave-induced stress may increase the friction velocity at $6\,\mathrm{m}$ amsl, and therefore, a lower-than-expected ϕ_w.~~

~~For an unstable atmosphere ($\zeta < 0$), the values of ϕ_w estimated at $18\,\mathrm{m}$ remain under **??**, which were not observed on FINO1 (Cheynet et al., 2018). It is unclear whether the lower-than-expected value of ϕ_w is due to the contribution of wave-induced stress to u_* or an underestimation of w' due to probe-induced flow-distortion. At $18\,\mathrm{m}$ amsl, the ratio S_w/S_u converges toward 1.2 in near-neutral conditions, i.e. slightly below the theoretical value of 1.33 (Kolmogorov, 1941). However, this value is similar to the ratio estimated from data measured at FINO1 platform. Therefore, the sensor-induced flow distortion is unlikely to explain the deviation between **??** and the estimated values at $18\,\mathrm{m}$ amsl. At $6\,\mathrm{m}$ amsl, the values of ϕ_w are fairly constant because the local estimate of ζ shows a great portion of near-neutral conditions than at $18\,\mathrm{m}$ amsl.~~

~~Friction velocity estimated by the three sonic anemometers on SMW for a wide range of stability conditions with $|\zeta| < 2$. Variation of the $\phi_w = \sigma_w/u_*$ with the non-dimensional Obukhov length ζ estimated from SA at $18\,\mathrm{m}$ amsl, superposed with the empirical value (black line) provided by Kaimal and Finnigan (1994). The error bar represents the interquartile range.~~

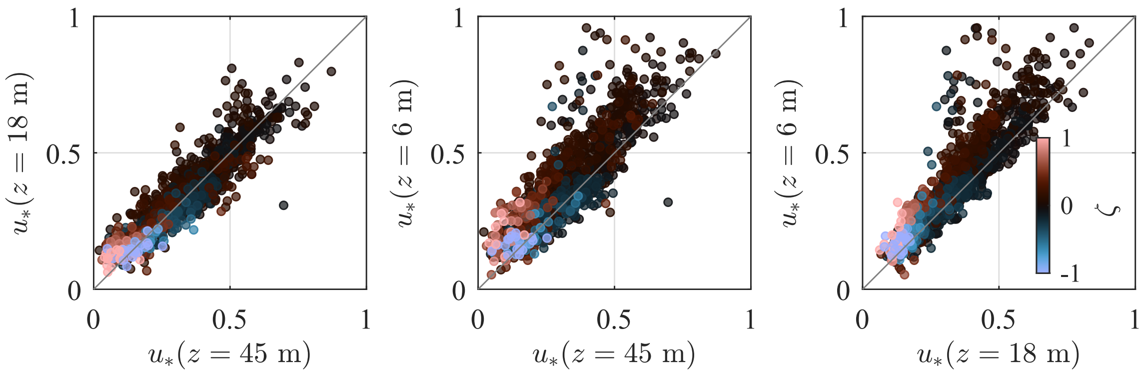

Figure 4. Friction velocity estimated by the three sonic anemometers on SMW for a wide range of stability conditions with $|\zeta| < 2$.

~~Variation of ϕ_m with the non-dimensional Obukhov length ζ estimated from SA at $18\,\mathrm{m}$ amsl. The solid black line is eq. (4) and the error bar represents the interquartile range.~~

~~The similarity relations~~ The similarity relation describing the mean wind speed profile agrees well with the sonic anemometer measurements under all stability conditions except between the sensor at $6\,\mathrm{m}$ and $18\,\mathrm{m}$ amsl at $\zeta > 0.3$. ~~In ??, the friction velocity is averaged between the two heights selected. Therefore, the observed deviation may be partly due to the contribution of the wave-induced stress to the friction velocity~~It should be noted that at $6\,\mathrm{m}$ amsl, the local estimate of ζ shows a much greater portion of near-neutral conditions than at $18\,\mathrm{m}$ amsl. The right panel of fig. 5 does not show such a deviation, maybe because the friction velocity estimated at $45\,\mathrm{m}$ amsl is slightly underestimated due to the high-frequency ~~noises~~ noise in the velocity records of the top sensor. ~~The turbulence measurement collected at $6\,\mathrm{m}$ amsl appears to be affected during a substantial amount of the time by the waves, which leads to clear deviations from MOST.~~ This further justifies the use of the sonic anemometer at $18\,\mathrm{m}$ amsl to estimate the non-dimensional ~~Obukhov length~~ stability parameter ζ.

~~A better agreement between the estimates and the empirical values of ϕ_m and ϕ_w is obtained if the friction velocity at $18\,\mathrm{m}$ amsl is used instead of the local values. Even when doing so, the estimated values of ϕ_w at $6\,\mathrm{m}$ amsl deviate from MOST. The validity of MOST in the vicinity of the sea surface under wind-sea conditions is, therefore, more disputed in the present case than in previous studies (e.g. Drennan et al., 1999).~~

The distribution of ζ as a function of the mean wind speed $\overline{u}$ is given in fig. 6 for the sector between 220° and 330°. The majority (82%) of the stationary records samples were associated with a wind speed between $7\,\mathrm{m\,s^{-1}}$ to $15\,\mathrm{m\,s^{-1}}$ at $18\,\mathrm{m}$ amsl. Non-neutral conditions are defined herein as situations where $|\zeta| > 0.1$. They represent 69% of the samples at $\overline{u} < 12\mathrm{m\,s^{-1}}$ and 12% at $\overline{u} \geq 12\mathrm{m\,s^{-1}}$. The distribution of the atmospheric stability conditions is in overall agreement with Barthelmie (1999) and Sathe and Bierbooms (2007) for Vindeby site.

5.2 ~~Local isotropy~~

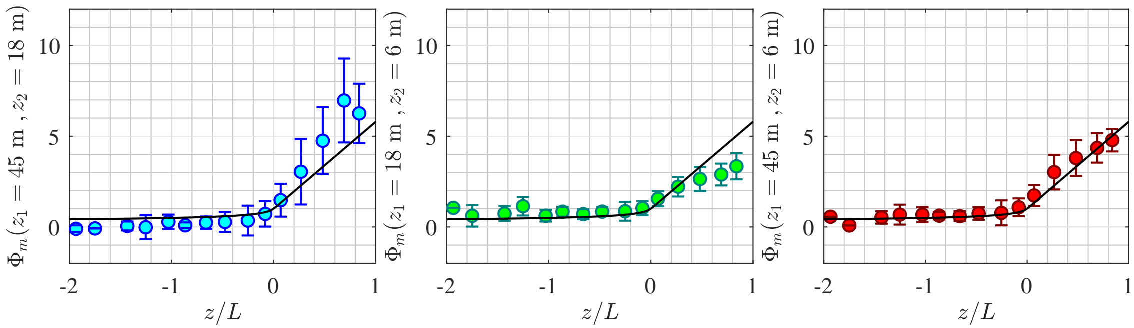

Figure 5. Variation of ϕ_m with the non-dimensional stability parameter ζ estimated from SA at 18 m amsl. The solid black line is eq. (4) and the error bar represents the interquartile range.

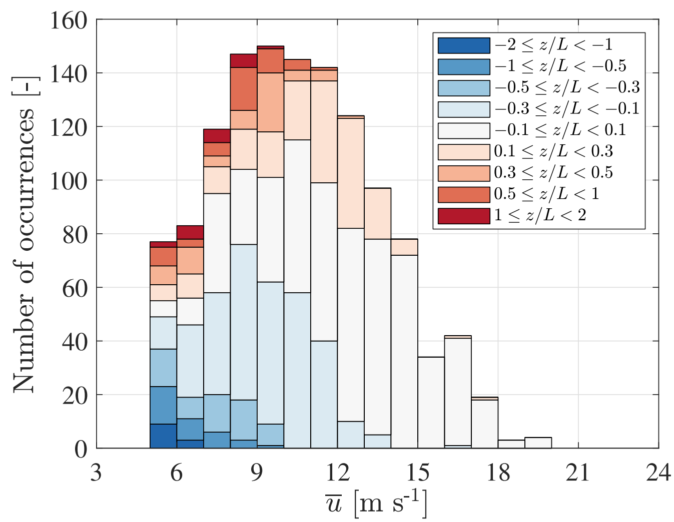

Figure 6. Stability distribution as a function of mean wind speed for the considered fetch (220°-330°) at height $z = 18\,\mathrm{m}$.

~~The~~ The local isotropy is evaluated by the spectral ratios S_v/S_u and S_w/S_u for near-neutral conditions ($-0.1 \leq \zeta \leq 0.1$). The spectral ratios are presented in fig. 7. As documented by e.g. Chamecki and Dias (2004), Cheynet et al. (2018) or Peña et al. (2019), the ~~isotropic values of~~ ratio S_v/S_u ~~are reached~~ reaches isotropy more easily than ~~by~~ S_w/S_u. The presence of significant measurement ~~noises~~ noise in the velocity data at the top sensor leads to ratios S_v/S_u and S_w/S_u that reach a maximum at $f_r \approx 3$ before decreasing at higher frequencies. The isotropic values of S_w/S_u are only reached for the sensors located at $6\,\mathrm{m}$ amsl. Smedman et al. (2003) observed that the maximum value of S_w/S_u is close to or below unity in the presence of a swell sea-state. Figure 7 shows that a similar deduction is not applicable here, because the wind-sea conditions are predominant. At $18\,\mathrm{m}$ amsl, the ~~maximum value of the~~ ratio S_w/S_u converges toward 1.2 in near-neutral conditions, i.e. slightly below the theoretical value of 1.33 (Kolmogorov, 1941). This value is similar to ~~those observed in Cheynet et al. (2018) or~~ the ratio estimated from data

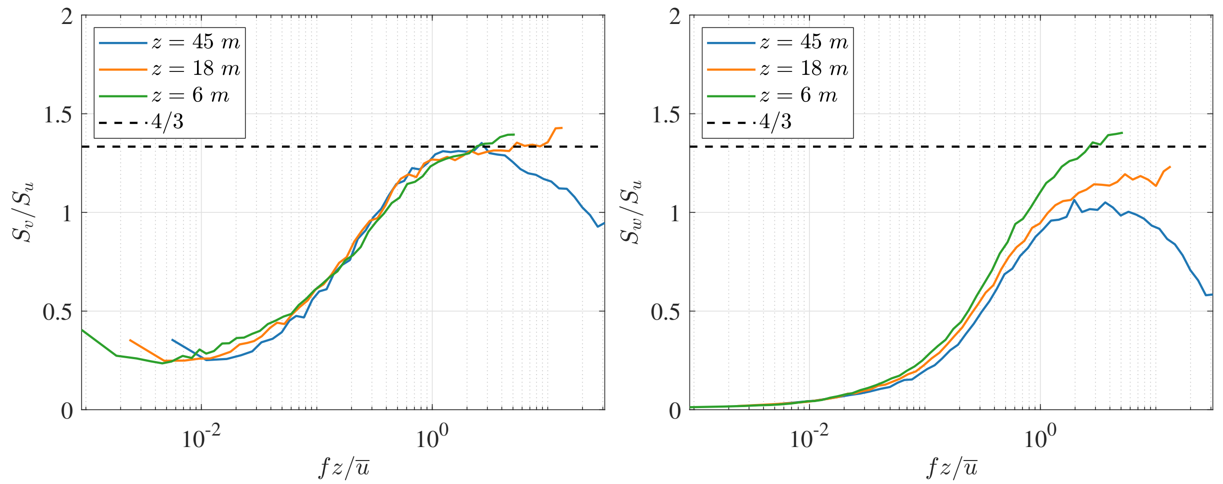

Figure 7. Spectral ratio S_v/S_u (left panel) and S_w/S_u (right panel) for near-neutral conditions. The dashed line represents the theoretical 4/3 value associated with local isotropy in the inertial subrange.

measured at FINO1 (Cheynet et al., 2018) or in Peña et al. (2019) and can be attributed to flow distortion by the instrument. ~~It is quite remarkable that the isotropic value of S_w/S_u is reached by the sensor closest to the surface, where flow distortion by the tower structure is usually larger than at the upper levels.~~

5.2 ~~Estimation of the friction velocity~~

~~Figure A1 compares the friction velocity estimates u_{*R} by Klipp (2018) and u_* when applying the double rotation of the anemometer axes for various atmospheric stratifications. In general, the resulting friction velocity from both methods is in good agreement. The average correlation coefficient for all heights is 0.985 for $|\zeta| \leq 2$. The PF algorithm leads to a slightly larger scatter between u_{*R} and u_*, where the average correlation coefficient from all heights is 0.976 for $|\zeta| \leq 2$ (Table A1) . The double rotation algorithm seems to give a smaller deviation between u_{*R} and u_* than the PF algorithm in the present study, which justified the adoption of the double rotation as tilt correction method herein.~~

~~noted that u_{*R} is appropriate to estimate the friction velocity if the thermal stratification of the atmosphere is neutral only. Yet, fig. A1 suggests that Klipp's method is performing well for non-neutral conditions too, as highlighted by the correlation coefficients in Table A1, which vary between 0.963 to 0.989. Additional studies using measurements from other coastal or offshore sites are needed to assess if such observations are recurring.~~

5.2 Wind-wave interactions

~~Correlation coefficients between u_{*R} and u_* using the planar fit (PF) or double rotation (DR) 6 m 18 m 45 m 6 m 18 m 45 m PF 0.989 0.976 0.962 0.981 0.954 0.942 DR 0.995 0.986 0.973 0.989 0.968 0.963~~

~~Friction velocity computed using the eddy covariance method with the double rotation method compared with the Klipp method. The upper panel considers only $|z/L| \leq 0.1$ and the lower panel considers $0.1 < |z/L| \leq 2$. Friction velocity computed using the eddy covariance method with the double rotation method compared with the Klipp method. The left panel considers only $|z/L| \leq 0.1$ and the right panel considers $0.1 < |z/L| \leq 2$.~~

~~The angle between the stress vector and the wind vector is given as $\alpha = \arctan\left(\overline{v'w'}/\overline{u'w'}\right)$ (Grachev et al., 2003). It is found that α increases from 8°~~ The close proximity of the sensor at $6\,\mathrm{m}$ with the sea surface is used to study the potential influence of the wave boundary layer (WBL) (Sjöblom and Smedman, 2003a). This layer is also called the wave sublayer by Emeis and Türk (2009), who suggest that its depth is approximately $5H_s$, although there is no consensus on the depth of the WBL. The objective of this subsection is to identify whether the wave-induced turbulence can be detected in the velocity records at $6\,\mathrm{m}$ amsl ~~to 13° at $45\,\mathrm{m}$ amsl when $\overline{v'w'} < 0$. When $\overline{v'w'} > 0$, α is almost constant with the height with an average value of $-7°$. The relatively low value of α therefore suggests that the direction of the wind-wave-induced stress is fairly well aligned with the mean wind direction near SMW.~~

5.3 ~~Wind-wave interactions~~

due to the observed turbulence characteristics in section 5.1.

~~The unusual turbulence characteristics identified at $6\,\mathrm{m}$ amsl in section 5.1are explored herein~~ Here, the measurements are explored in terms of wind-wave interactions, using the wave elevation data collected by the ~~acoustic wave recorder~~ AWR near SMW. A total of 925 high-quality samples collocated in time with the wind velocity data studied ~~herein~~ were identified. Each wave elevation record was $30\,\mathrm{min}$ long and corresponded to a wind direction between 220° and 330°. There exist methods to filter out the wave-induced velocity component from the turbulent velocity component (e.g. Hristov et al. (1998)), but these methods are not addressed herein for brevity.

The term “high-quality samples” refers to the sea surface elevation time histories $\eta(t)$ without flattened valleys or significant measurement noises at frequencies under $f_t = 0.10\,\mathrm{Hz}$, which were sometimes observed in the records. The identified wave peak period T_p was generally located at frequencies above $0.20\,\mathrm{Hz}$, which justifies the choice of a threshold frequency of $0.10\,\mathrm{Hz}$. More precisely, the contribution of wave elevation data at frequencies below f_t to the variance of the signal was negligible unless non-stationary fluctuations were recorded. The sea surface elevation skewness ranged from -0.02 to 0.37 with a median value of 0.17, while the kurtosis varied from 2.7 to 3.4 and a median value of 3. Therefore, ~~eta~~ η time series can be assumed Gaussian on average and the significant wave height H_s was approximated as $4\sigma_\eta$ where σ_η is the standard deviation of the sea surface elevation (Longwet-Higgins, 1952). Nonetheless, it should be ~~emphasized~~ emphasised that these results are concluded based on the measurement at one location near SMW, and the wave characteristics upstream of the mast are unexplored.

Hourly hindcast data with a $2\,\mathrm{km}$ horizontal resolution (Tuomi and Huess, 2020) ~~gives~~ give larger H_s values than the measurement data as shown in fig. 8. Close to the coast and in shallow water areas, the accuracy of hindcast data is usually lower~~. Also,~~ , while the relatively low accuracy of the wave measurements leads to underestimated H_s values. ~~Nevertheless, the~~ The measured significant wave heights were below $1.5\,\mathrm{m}$ during 1994 and 1995 with a median value of $0.4\,\mathrm{m}$. The hindcast

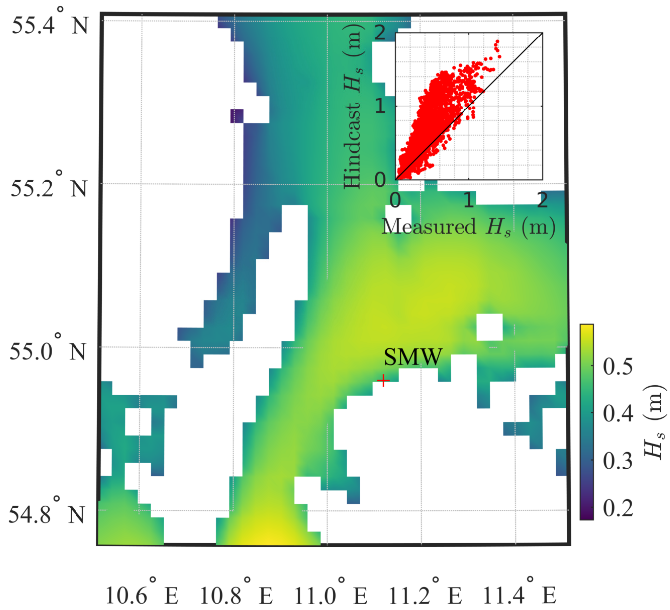

Figure 8. ~~Co-coherence $\gamma_{\dot{\eta}w}$ and quad-coherence $\rho_{\dot{\eta}w}$ between the velocity~~ Median value of the hourly significant wave ~~surface $\dot{\eta}$ and the vertical wind velocity w from~~ height for the ~~three sonic anemometers on~~ year 1995 near SMW provided by the hindcast data (Tuomi and Huess, 2020). The inset ~~shows~~ compares the ~~individual wave elevation spectra S_η associated with $H_s > 0.9\,\mathrm{m}$ (60 samples) used to estimate $\gamma_{\dot{\eta}w}$~~ measured and ~~$\rho_{\dot{\eta}w}$.~~ modelled H_s values between 1994 and 1995.

data provided H_s values for wind-sea, primary and secondary swell. These data indicated that wind-sea conditions were largely predominant over swell conditions, ~~as already mentioned in ??~~nearby SMW.

The interactions between wind turbulence and the sea surface were explored in terms of the co-coherence and the quad-coherence (the imaginary part of the root-coherence) between the vertical velocity component w and the velocity of the wave surface $\dot{\eta} = \mathrm{d}\eta/\,\mathrm{d}t$. Similar approaches were adopted earlier by e.g. Grare et al. (2013) or Kondo et al. (1972) but using the ~~squared~~ coherence and without taking advantage of the ensemble average to reduce the systematic and random error, which are typically associated with the ~~coherence~~ root-coherence function. In the present case, ~~no clear coherence was found~~ neither the co-coherence nor the quad-coherence between $\dot{\eta}$ and w differs significantly from zero for $H_s < 0.7\,\mathrm{m}$. For the sensor at $6\,\mathrm{m}$ amsl, a non-zero ~~coherence~~ root-coherence was discernible from the background noise at $0.7\,\mathrm{m} < H_s < 0.9\,\mathrm{m}$. The co-coherence and quad-coherence estimates were significantly different from zero for ~~$0.9\,\mathrm{m} \leq H_s$~~$0.9\,\mathrm{m} \geq H_s$, as illustrated in fig. 9, where the ensemble averaging of the 60 samples was applied to reduce the random error. The inset in fig. 9 shows that the selected records are ~~characterized~~ characterised by a single spectral peak f_p located at frequencies between $0.20\,\mathrm{Hz}$ and $0.25\,\mathrm{Hz}$, which is the frequency range where the quad-coherence is substantially different from zero. The observed ~~behaviour of the~~ co-coherence and the quad-coherence at this frequency range ~~may~~ show the 90° out-of-phase fluctuations between $\dot{\eta}$ and w,

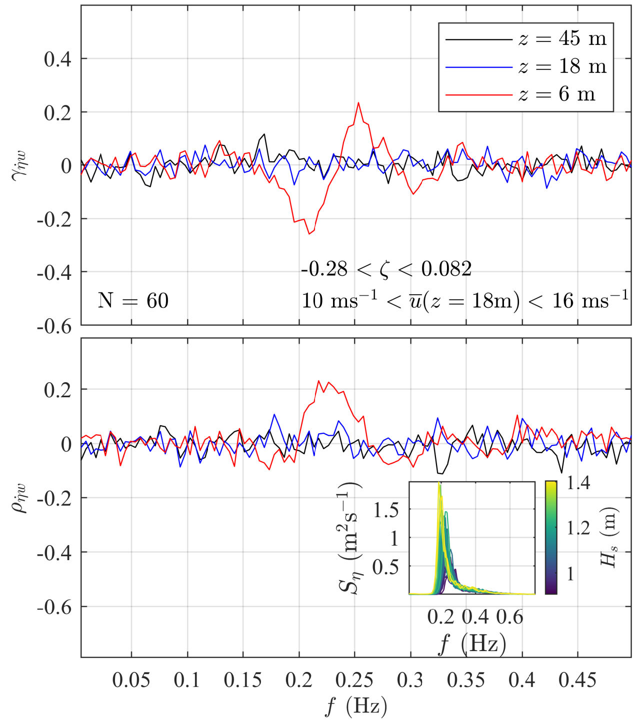

Figure 9. ~~Median value~~ Co-coherence $\gamma_{\dot{\eta}w}$ and quad-coherence $\rho_{\dot{\eta}w}$ between the velocity of the ~~hourly significant~~ wave ~~height for~~ surface $\dot{\eta}$ and the ~~year 1995 near SMW provided by~~ vertical wind velocity w from the ~~hindcast data (Tuomi and Huess, 2020)~~three sonic anemometers on SMW. The inset ~~compares~~ shows the ~~measured and modelled H_s values between 1994~~ individual wave elevation spectra S_η associated with $H_s > 0.9\,\mathrm{m}$ (60 samples) used to estimate $\gamma_{\dot{\eta}w}$ and ~~1995.~~$\rho_{\dot{\eta}w}$.

where the latter is lagging. The co-coherence and quad-coherence estimates between $\dot{\eta}$ and the horizontal wind component u were also investigated but were nearly zero for the three sonic anemometers on SMW.

~~It should be noted that the~~ The limited number of data showing a clear correlation between the velocity of the sea surface and the vertical wind component implies that the wave-induced turbulence has a limited impact on the anemometer records at $6\,\mathrm{m}$. The influence of the sea surface elevation on the vertical turbulence was not clearly visible in the one-point vertical velocity spectra S_w, except for $H_s > 1.2\,\mathrm{m}$, where a weak spectral peak near $0.2\,\mathrm{Hz}$ was distinguishable. The wave-induced fluctuating wind component is generally much less compared to the wind turbulence ~~(Weiler and Burling, 1967; Kondo et al., 1972; Naito, 1983)~~ as highlighted by e.g. Weiler and Burling (1967); Kondo et al. (1972); Naito (1983). An exception ~~is~~ may be the case of weak wind and swell conditions which are more likely to result in the observation of a sharp spectral peak near f_p in the S_w spectrum (Kondo et al., 1972). Nonetheless, as previously mentioned, such conditions are rare near SMW~~.~~, most likely because SMW was located in a relatively sheltered close-water environment rather than an open ocean.

~~According to Grare et al. (2013), the contribution of wave-induced momentum flux to the total momentum flux $\overline{u'w'}$ is positive for relatively young waves, i.e. $C_p/u_* < 40$, where C_p is the phase speed at the wave spectral peak. Using shallow water theory, the wave age near SMW is $C_p/u_* < 30$ most of the time, which would partly explain the larger friction velocity measured at 6 m amsl compared to 18 m amsl. It should be noted, however, that the study by Grare et al. (2013) was conducted in deep waters with measurements located at heights lower than $5H_s$. They noted that the positive contribution of the wave-induced momentum flux they measured was close to or below 10% of the total momentum flux. In the present case, the sonic anemometers were located at heights close to or larger than $5H_s$ most of the time. Nevertheless, the momentum flux $\overline{u'w'}$ estimated at 6 m amsl was, on average, 21% and 18% larger than those at 45 m and 18 m, respectively. For stable conditions with $\zeta > 0.2$, $\overline{u'w'}$ at 6 m was 50% larger than at 45 m amsl and 18 m amsl. Both results displayed in **??** and fig. 9 suggest that the wave sublayer, as defined by Emeis and Türk (2009), may be deeper than $5H_s$ near SMW.~~

~~The limited number of data showing a clear correlation between the velocity of the sea surface and the vertical wind component may imply that the deviations from MOST observed at 6 m amsl may also be influenced by the heterogeneous surface roughness nearby SMW. For the wind sectors selected, an increase in the average H_s toward SMW can be seen in fig. 8. This would result in spatially-varying surface roughness between the upstream region and nearby SMW. In shallow water close to SMW (up to 300 m), it is likely to observe the presence of non-linear wave steepness that would contribute to enhanced surface roughness and thus larger turbulent stresses in the proximity of the mast. The variability of the surface roughness may be small enough so that ϕ_m follows MOST at 6 m amsl but not ϕ_w. The latter is based on local measurements only and is, therefore, more sensitive to a height-dependant friction velocity than ϕ_m.~~

5.3 Turbulence spectra

When performing numerical simulations to compute the wind-induced response of wind turbines, an essential input to model the wind inflow conditions is the PSD of the velocity fluctuations. Figure 10, fig. 11, and fig. 12 depict the PSD estimates respectively for the along-wind, cross-wind, and vertical ~~velocity~~ wind components as a function of the ~~reduced frequency $f_r = fz/\overline{u}$~~ reduced frequency f_r for nine stability classes. Surface-layer scaling is adopted, i.e. the PSDs are ~~normalized~~ normalised with u_* (eq. (2)) and $\phi_\epsilon^{2/3}$ (~~eq. (7)~~eq. (8)). Strongly non-neutral cases, defined as $|\zeta| > 2$ are not studied herein as they are fairly uncommon for the ~~dataset~~ data-set selected. The number of available samples for each stability class is denoted as N and displayed in each sub-panel.

These three figures compare the estimated spectra at $z = 45\,\mathrm{m}$, $z = 18\,\mathrm{m}$, and $z = 6\,\mathrm{m}$ amsl with the empirical model established on ~~the~~ FINO1 ~~platform~~ (black solid line) at ~~$z = 41.5\,\mathrm{m}$~~ $z = 41\,\mathrm{m}$ amsl (Cheynet et al., 2018). The red curves represent the high-frequency asymptotic behaviour of surface-layer spectra for each stability class. It should be noted that the latter curves do not indicate when the inertial subrange starts since the frequencies they cover were arbitrarily chosen.

In fig. 10, the maximum values of the ~~normalized~~ normalised spectra for near-neutral conditions are close to unity, as described by Kaimal et al. (1972)~~which is another indication that the friction velocity was estimated properly. As highlighted in **??**, the anemometer at 6 m amsl recorded a friction velocity significantly larger than at 18 m amsl and 45 m amsl, which introduces a deviation from eq. (5) when the surface-layer scaling is applied to the velocity spectra. As mentioned in section 5.2, no spectral~~

~~peak around the wave spectral peak f_p is visible in the S_w spectrum, as expected, since ensemble averaging is applied and that such events were hardly observed at Vindeby.~~

~~As sketched in fig. 10, the~~. The velocity spectra estimated at 45 m amsl show ~~systematic deviations from MOST~~ sometimes deviations from the surface-layer scaling under near-neutral and stable conditions, likely due to the observed aforementioned uncorrelated high-frequency ~~noises~~noise, which lead to an underestimation of the friction velocity. Under light and moderate unstable conditions, i.e. $-0.3 \le \zeta \le -0.1$, the velocity spectra at 6 m and 18 m amsl are similar, which supports the idea that the wave sublayer is shallower than 6 m. If $\zeta \le -1$, deviations from ~~MOST~~ surface-layer scaling are clearer at both 45 m ~~amsl~~ and at 6 m~~amsl~~, which is also visible in fig. 12. We remind that the non-dimensional stability parameter ζ estimated at 6 m reflected the predominance of near-neutral conditions. This results in discrepancies between the spectral estimates at 6 m and 18 m in fig. 10 to fig. 12 which increase with $|\zeta|$.

Following ~~MOST, the normalized~~ surface-layer scaling, the normalised spectra at different heights should collapse onto one single curve at high frequencies, which was observed at heights between 40 m amsl and 80 m amsl at ~~the~~ FINO1 ~~platform~~ for $|\zeta| < 1$. However, this is not always the case in fig. 10, fig. 11, and fig. 12. ~~Deviations from MOST for the PSDs estimates at 6 m amsl were expected due to the contribution of wave-induced momentum flux (section 5.1)~~Deviations from surface-layer scaling may be partly attributed to transducer-induced flow distortion. Regarding the velocity data at 45 m amsl, the measurement noises lift the high-frequency range of the velocity spectra above the spectral slope predicted by eq. (5) or eq. (6). At 18 m amsl, eqs. (5) and (6) predict remarkably well the velocity spectra at $f_r > 3$, indicating that surface-layer scaling is applicable at this height.

The presence of the spectral gap (Van der Hoven, 1957), separating the microscale fluctuations from the sub-meso and mesoscale ones, is noticeable at $\zeta > 0.3$, in line with previous observations (Smedman-Högström and Högström, 1975; Cheynet et al., 2018). Under stable conditions, the spectral gap seems to move toward lower frequencies as the height above the surface decreases. This contrasts with the observations from an onshore mast on Østerild (Denmark) by Larsén et al. (2018), which indicated that the location of the spectral gap on the frequency axis was relatively constant with height.

Following Vickers and Mahrt (2003) the spectral gap timescale can be only a few minutes long under stable conditions. For $\zeta > 0.5$, the averaging period selected in the present study may be too large to provide reliable integral turbulence characteristics. However, filtering out the mesoscale motion may not be desirable for structural design purposes since operating wind turbines experience both turbulence and mesoscale fluctuations (Veers et al., 2019). In this regard, the use of spectral flow characteristics to parametrise the wind loading on OWTs is preferable.

Under near-neutral conditions, the sensors at 6 m amsl and 18 m amsl are likely located in the so-called eddy surface layer (Högström et al., 2002; Drobinski et al., 2004), where the sea surface blocks the flow and distorts eddies. This leads to a flat spectral peak~~because~~. As a result, the integral length scale ~~cannot be easily estimated~~ would be estimated with large uncertainties. Such a spectral behaviour has also been observed above the eddy surface layer (Drobinski et al., 2004; Mikkelsen et al., 2017) but its consequences on wind turbine loads are unclear.

~~Deviations from the~~ Deviations from surface-layer scaling at $\zeta > 0.5$ ~~are mainly~~ may be due to the ~~contribution of wave-induced stress to the total turbulent shear stress. This contribution was found to be highest for stable conditions compared to neutral andunstable ones (fig. 4).~~fact that the sensors are no longer located in the surface layer and/or that transducer-induced flow

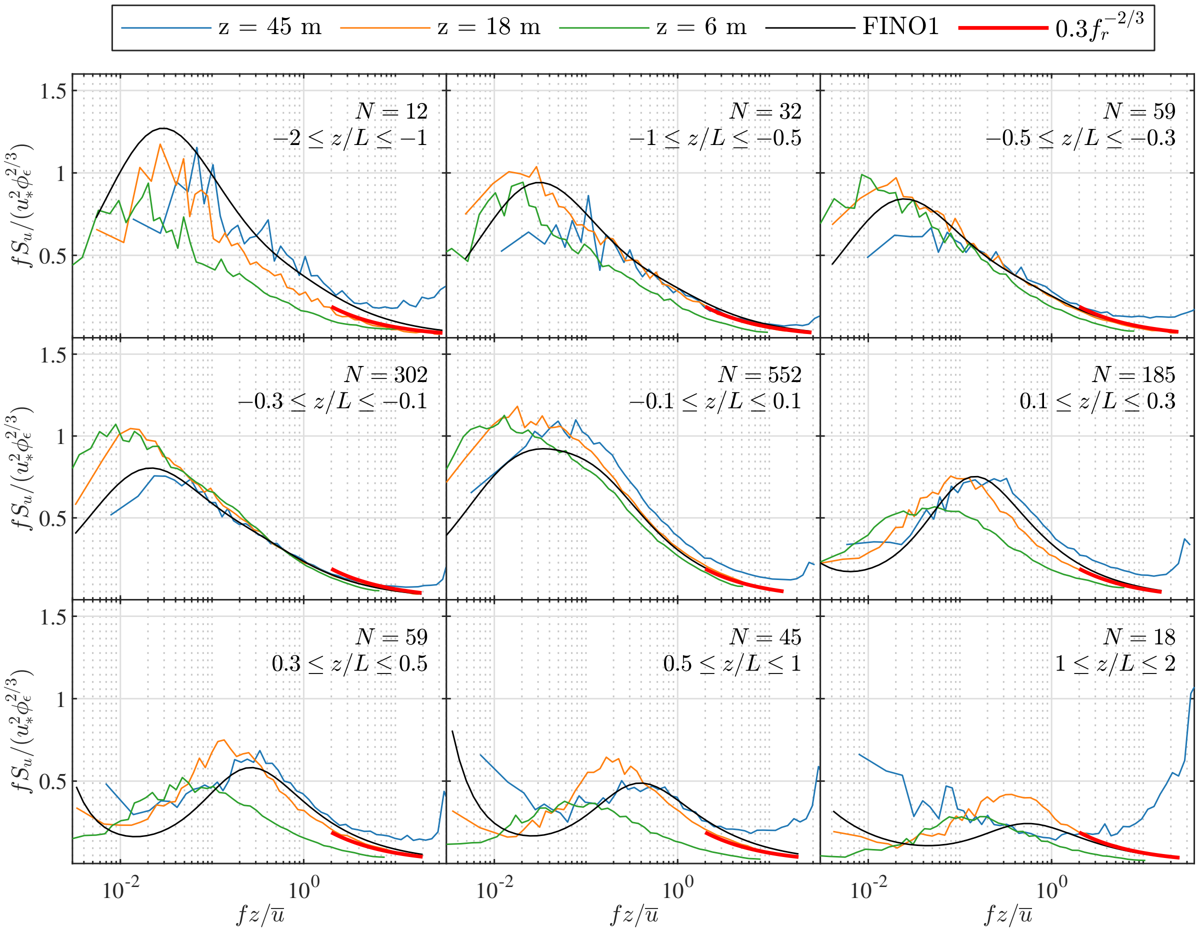

Figure 10. ~~normalized~~ Normalised spectra of the along-wind component at ~~45 m, 18 m and 6 m~~ 45, 18, and 6 m amsl for various stability conditions. The red curve is derived from eq. (5) ~~for reference but does not necessarily reflect~~ and N denotes the ~~presence~~ number of ~~an inertial subrange in the data~~samples considered for ensemble averaging.

distortion is not negligible. For $\zeta > 1$, further deviations from ~~MOST~~ surface-layer scaling may be related to the so-called local z-less stratification (Wyngaard and Coté, 1972) where turbulence is no longer scaled by the height above the ground.

Overall, the velocity spectra estimated at 18 m amsl and 45 m amsl at Vindeby match reasonably well with the empirical spectra estimated at 41 m amsl on ~~the~~ FINO1 ~~platform for $-2 \geq \zeta < 1$~~for $-2 \leq \zeta \leq 1$. This comparison is encouraging for further explorations of the surface-layer turbulence characteristics at coastal and offshore sites. Nonetheless, detailed wind measurements at ~~altitudes~~ heights $z \geq 100$ m are ~~favoured~~ needed to get a complete overview of the turbulence characteristics in the MABL that ~~could be~~ is relevant for OWT designs.

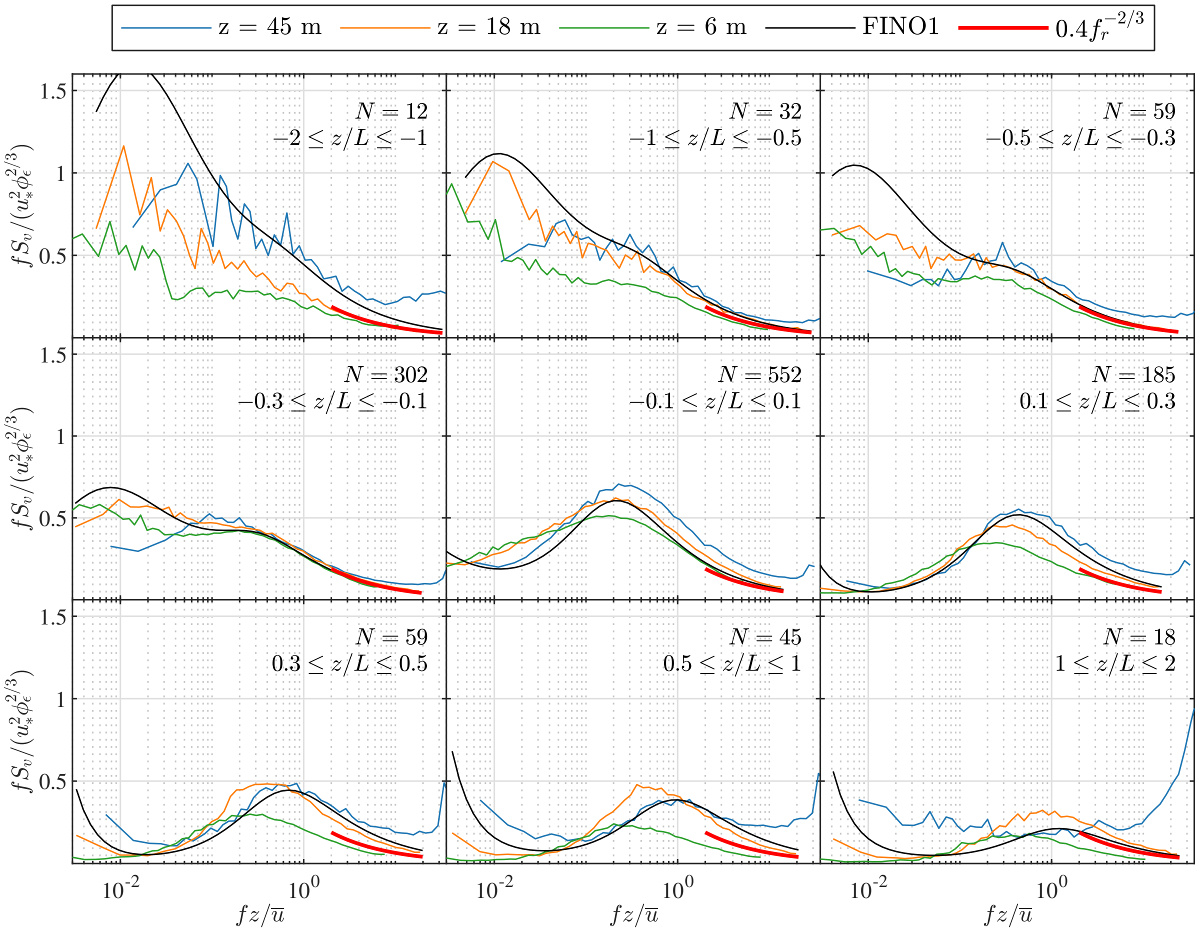

Figure 11. ~~normalized~~ Normalised spectra of the cross-wind component at ~~45 m, 18 m and 6 m~~ 45, 18, and 6 m amsl for various stability conditions. The red curve is derived from eq. (6) ~~for reference but does not necessarily reflect~~ and N denotes the ~~presence~~ number of ~~an inertial subrange in the data~~samples considered for ensemble averaging.

5.4 Co-coherence of turbulence

The vertical co-coherence of the along-wind, cross-wind, and vertical wind components are denoted ~~as~~ by γ_u, γ_v, and γ_w, respectively. Under near-neutral conditions ($|\zeta| \leq 0.1$), these are expressed as a function of kd_z in fig. 13 where $k = 2\pi f/\overline{u}$ ~~using the assumption of frozen turbulence~~ is the wave number, assuming that turbulence is frozen (Taylor, 1938). The co-coherence estimates are presented for three separation distances d_z ~~as~~ because three measurement heights ($z_1 = 45\,\mathrm{m}$, $z_2 = 18\,\mathrm{m}$, and $z_3 = 6\,\mathrm{m}$) were used. The co-coherence ~~estimates collected~~ estimated on SMW are compared to the IEC coherence model (eq. (15)) and the modified Bowen model (eq. (14)). For the latter model, the parameters estimated on ~~the~~ FINO1 ~~platform (Cheynet, 2019)~~ (Cheynet, 2019) are directly used~~since we aim to assess how similar are the turbulence characteristics~~

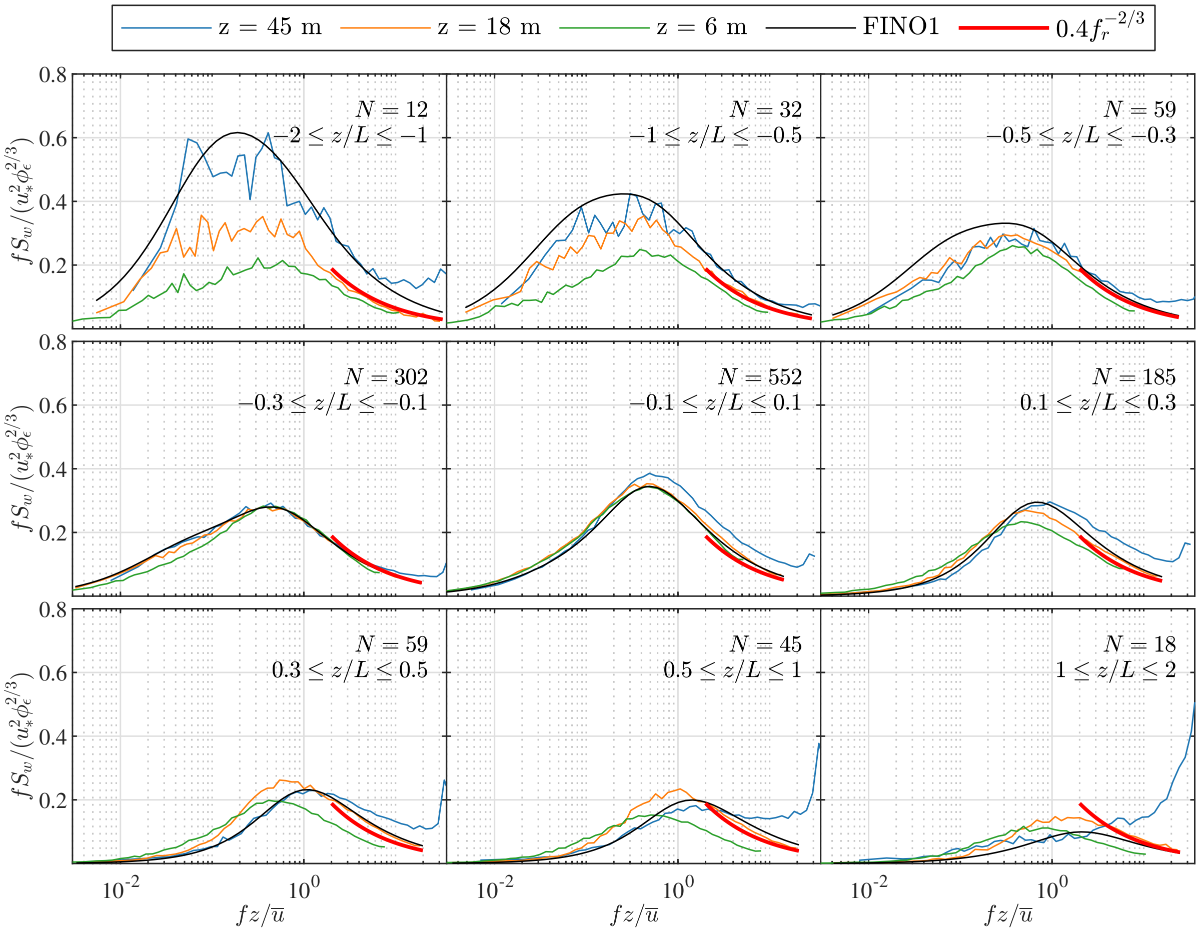

Figure 12. ~~normalized~~ Normalised spectra of the vertical wind component at ~~45 m, 18 m and 6 m~~ 45, 18, and 6 m amsl for various stability conditions. The red curve is derived from eq. (6) ~~for reference but does not necessarily reflect~~ and N denotes the ~~presence~~ number of ~~an inertial subrange in the data~~samples considered for ensemble averaging.

~~of the atmosphere at FINO1 and Vindeby.The decay constants~~ . The decay coefficients used for eq. (14) were, therefore, $[c_1^u, c_2^u, c_3^u] = [6.0, 17.8, 0.02]$ and $[c_1^w, c_2^w, c_3^w] = [2.7, 4.0, 0.16]$ as well as ~~$[c_1^v, c_2^v, c_3^v] = [0, 23, 0.09]$~~ $[c_1^v, c_2^v, c_3^v] = [0, 23.0, 0.09]$.

Figure 13 shows that the coefficients of the modified Bowen model estimated on ~~the~~ FINO1 ~~platform apply exceptionally~~ apply very well to γ_u estimated on SMW. Larger deviations are observed for the cross-wind components, for which γ_v displays large negative values, especially for separations between 6 m amsl and 45 m amsl. On ~~the~~ FINO1~~platform~~, the negative part of γ_v was relatively small, which justified the use of eq. (14) with no negative co-coherence values. Following Bowen et al. (1983); ESDU 85020 (2002) or Chougule et al. (2012), the negative part is a consequence of the phase difference ~~,~~ and is non-negligible for the cross-wind component, which is also observed in the present case. Since this phase difference increases with the mean

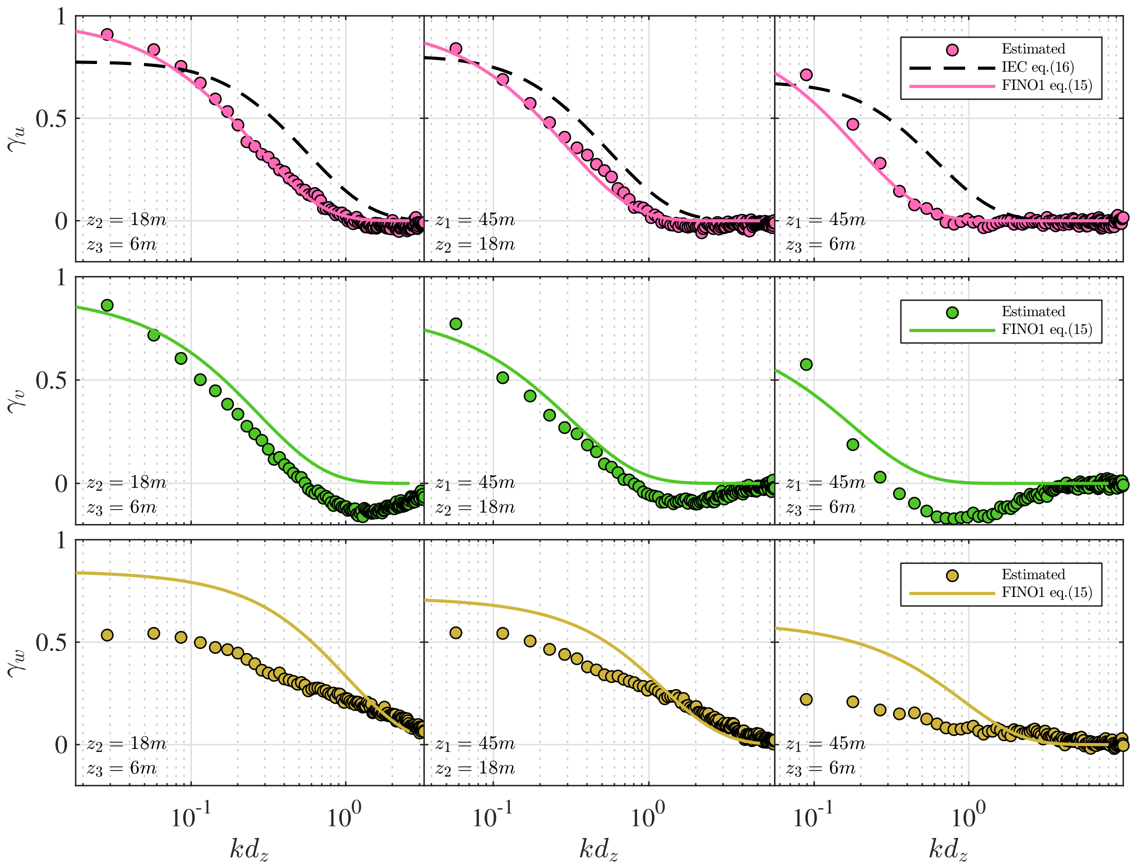

Figure 13. Co-coherences of the along-wind (top panels), lateral (middle panels), and vertical velocity components (lower panels) for $|\zeta| \leq 0.1$ at three different ~~d_z~~ vertical separation distances. The dots represent the measurement and the lines mark the ~~empirical values computed~~ predictions using the IEC exponential coherence model (dashed line) and the Modified Bowen model (solid line) with the fitted coefficients from FINO1 (Cheynet, 2019).

wind shear, it is more visible at SMW than at FINO1, where the measurements are at ~~higher altitudes~~ greater heights than at SMW.

The IEC exponential coherence model over-predicts γ_u when the measurement height decreases and when the separation distance increases because this model follows fairly well Davenport's similarity, except at $kd_z < 0.1$. In Cheynet (2019), the Davenport model was suspected to lead to an overestimation of the turbulent wind loading on OWTs. The present results indicate that a similar overestimation may be obtained if the IEC exponential coherence model is used. Further studies are, however, needed to better quantify this possible overestimation ~~since the lateral~~ in terms of dynamic wind loading on the wind turbine's rotor and tower, as well as on the floater's motions in the case of a floating wind turbine. Finally, additional data collection is needed to study the co-coherence ~~is also required but could not be obtained~~ at lateral separations, which is required for wind turbine design since it was not available at FINO1 nor SMW.~~The co-coherence for lateral separations may~~

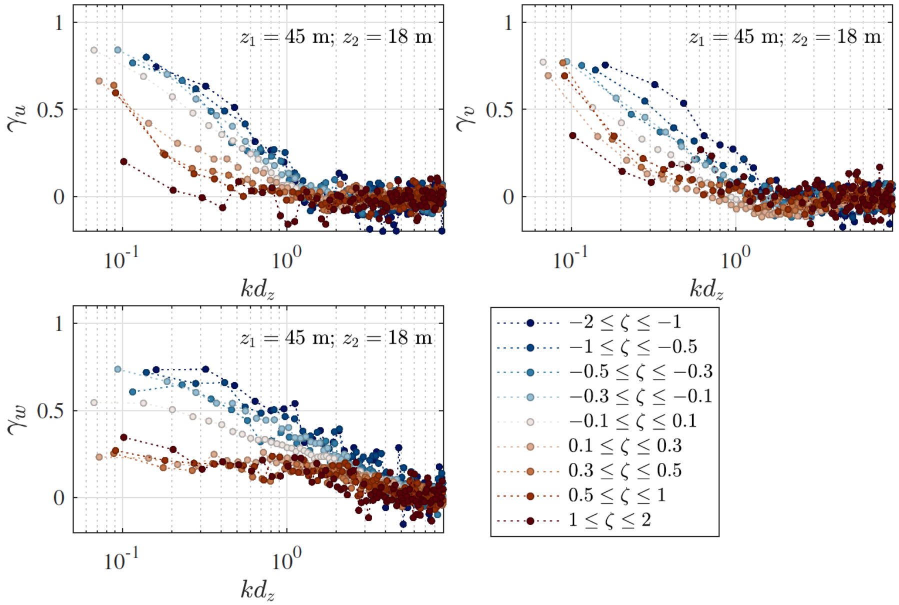

Figure 14. ~~Co-coherences at separation between z_1~~ Co-coherence of the along-wind (top left), cross-wind (top right) and ~~z_2~~ vertical (bottom-left) velocity components for ~~varying z/L~~ nine stability classes, given by $\zeta 0z/L$. The ~~upper left panel shows the estimated γ_u~~ separation distance is 27 m, between the ~~right upper panel displays the estimated γ_v,~~ sensors at 18 m and ~~the bottom left panel presents the estimated γ_w~~ 45 m amsl.

~~be obtained using Doppler wind lidar instruments (Cheynet et al., 2016, 2021) or wind sensors mounted on unmanned aerial vehicles (Wetz et al., 2021; Vasiljević et al., 2020) since deploying multiple masts at offshore is likely too costly.~~

Figure 14 shows a clear variation of the estimated co-coherence with thermal stratification of the atmosphere for the three turbulence components. As observed by e.g. Soucy et al. (1982) or Cheynet et al. (2018) and modelled by Chougule et al. (2018), the vertical co-coherence is generally highest for convective conditions and smallest for stable conditions. Such results reinforce the idea that modelling the turbulent loading on offshore wind ~~turbine~~ turbines using a coherence model established for neutral conditions may only be appropriate for the ultimate limit state design but not for the fatigue life design.

6 ~~Relevancy of the database for load calculation of OWTs~~

5.1 Relevancy of the database for load calculation of OWTs

~~While the present study provided~~ This study provides a thorough overview of the MABL spectral turbulence characteristics with respect to the variation of the atmospheric stability at SMW. However, its direct applicability for the designs of OWTs ~~has several limitations.~~ should be assessed carefully due to the assumptions made in the data analysis.

~~The first one is related to the fact that the~~ The presented results do not include the non-stationary conditions encountered in the field, which were removed before the analysis. About 20% of the data were disregarded as non-stationary to establish reliable spectra and co-coherence estimates. In the present case, non-stationary fluctuations were mainly associated with frequencies close to or below $0.05\,\mathrm{Hz}$. For typical spar-type and semisubmersible OWT floaters, these frequencies encompass the quasi-static motions and few lowest eigen-frequencies of the floaters (Jonkman and Musial, 2010; Robertson et al., 2014). Additionally, the non-stationary turbulence fluctuations could result in non-Gaussian loadings, which could further lead to underestimation of fatigue loading (Benasciutti and Tovo, 2006, 2007). ~~Therefore, direct use of the presented results for floater motions and load estimations of OWTs may be associated with additional uncertainties, which could be addressed by introducing a safety factor.~~

~~Secondly~~Furthermore, the present ~~dataset~~ data-set was recorded at heights lower than the hub height of the recent and the future OWTs, which is around $130\,\mathrm{m}$ (e.g. GE Renewable Energy, 2021). At such heights, MOST may no longer be applicable (Peña and Gryning, 2008; Cheynet et al., 2021). Above the surface layer, the velocity spectra ~~tend to be invariant with height, which is coarsely accounted for in IEC 61400-1 (2005) and suggested by preliminary observations from Doppler wind lidar instruments in coastal areas (Cheynet et al., 2021). Højstrup (1982) proposed an empirical turbulence spectral model for a convective boundary layer up to $0.5z_i$, where z_i is the convective boundary layer height (Wyngaard and Coté, 1972), that could be used to characterize turbulence~~ may become independent of the height above the surface~~layer. However, this model was not validated in the MABL, thus its applicability for OWT designs remains uncertain. For weakly stable atmosphere, turbulence can be parametrized using local similarity theory (Nieuwstadt, 1984; Sorbjan, 1986; Moraes, 1988), even though it is not known up to which height this approach is feasible in the MABL. Therefore, additional measurements at coastal and offshore sites complementing those from Vindeby or FINO1 are required to assess the validity of stability-dependant turbulence models for the design of tall offshore wind turbines~~, which is coarsely accounted for in IEC 61400-1 (2005).

6 Conclusions

This study explores the turbulence spectral characteristics from wind records of a year duration on an offshore mast called South Mast West (SMW) near the first offshore wind farm Vindeby. ~~This study aims~~ We aim to identify similarities between the turbulence characteristics estimated on the FINO1 platform ~~(North Sea)~~ in the North Sea and those at Vindeby. Such an investigation is crucial to establish appropriate turbulence models relevant for the design of offshore wind turbines (OWTs). The ~~dataset~~ data-set analysed was acquired by 3D sonic anemometers at ~~$6\,\mathrm{m}$, $18\,\mathrm{m}$ and $45\,\mathrm{m}$ above the~~ 6, 18, and $45\,\mathrm{m}$ above mean sea level (amsl), which complements the ~~dataset~~ data-set collected between $40\,\mathrm{m}$ and $80\,\mathrm{m}$ amsl on ~~the~~ FINO1 ~~platform~~ (Cheynet et al., 2018).

~~Although the non-dimensional mean wind speed profile seems to follow Monin-Obukhov similarity theory (MOST) between $6\,\mathrm{m}$ and $45\,\mathrm{m}$ amsl at SMW, the turbulence characteristics at $6\,\mathrm{m}$ amsl showed deviations from MOST, especially under neutral and stable conditions. The friction velocity measured at this height is substantially higher than at $18\,\mathrm{m}$ amsl and $45\,\mathrm{m}$ amsl. In this regard, the measurements at $6\,\mathrm{m}$ could be considered to be located in the wave sublayer, although a direct~~ The correlation between the sea surface elevation and the ~~turbulent fluctuations was observed for significant wave heights above 0.9 m only. This correlation was~~ vertical turbulent fluctuations at 6 m amsl is quantified in terms of co-coherence between the vertical ~~turbulence~~ turbulent component and the velocity of the sea surface ~~. The dominant contributor for the larger friction velocity at 6 m amsl may be the heterogeneous surface roughness that increases in the proximity of SMW.~~elevation. However, it is clearly visible for significant wave heights H_s exceeding 0.9 m only. Therefore, it is concluded that the sonic anemometers are located above the wave boundary layer most of the time.

The ~~velocity records~~ measurements at 18 m amsl follow fairly well ~~the~~ surface-layer scaling~~and their spectral characteristics are consistent with those from the measurement at FINO1 platform at 40 m amsl (Cheynet et al., 2018)~~, as expected. Because the ~~measurements~~ sensors at 6 m and 18 m ~~amsl~~ are located in the lower part of the surface layer, a wide spectral peak ~~at~~ for near-neutral stratification is observed, which reflects the distortion of the eddies as they scrape along the surface. ~~The turbulence spectra at 45 m amsl agree reasonably well with those from the~~ For $\zeta = |z/L| \leq 0.3$, the power spectral density of the along-wind velocity component at 18 m and 45 m are consistent with the empirically-defined spectral models estimated at 41 m on FINO1 ~~platform under convective conditions. For neutral and stable conditions~~ ~~$(-0.1 \leq \zeta \leq 1)$~~~~, both spectra at 45 m on SMW and 41.5 m at~~ (Cheynet et al., 2018). In the present case, most of the wind records are associated with $|\zeta| < 0.3$. Nonetheless, for $|\zeta| > 0.3$, deviations from the empirical spectral model fitted to the data recorded on the FINO1 ~~are especially similar, except in the high-frequency range, where measurement noise is prevailing at 45 m on SMW~~platform may be attributed to transducer-induced flow distortion and/or limited applicability of the surface-layer scaling.

The co-coherence estimates of the along-wind component for neutral atmospheres are ~~exquisitely~~ well-described by the same 3-parameter exponential decay function as used at FINO1 (Cheynet, 2019). However, this is not the case for the ~~cross-wind and the vertical~~ lateral wind components due to the closer distance to the sea surface which amplifies the phase differences between measurements at two different heights. For the vertical component, the co-coherence decreases faster than the predicted values at FINO1 (Cheynet et al., 2018). Under stable stratification, the co-coherence estimates of the three turbulent components (γ_u, γ_v, and γ_w) are significantly lower than for near-neutral conditions, in particular for $kd_z < 1$. On the other hand, γ_u, γ_v, and γ_w are slightly higher for convective conditions compared to near-neutral conditions at $kd_z < 1$. Since the co-coherence is one of the governing parameters for wind loading on structures, its dependency on the atmospheric stability, which is rarely documented in the marine atmospheric boundary layer may become essential to establish design criteria for OWT fatigue life. The variability of Hywind Scotland wind turbines' floater motion with atmospheric stability (Jacobsen and Godvik, 2021) may be one example that demonstrates the importance of stability-corrected co-coherence on OWT responses.

The comparison between the turbulence ~~data~~ characteristics at Vindeby and FINO1 is valuable to further develop comprehensive spectral turbulence models that are suitable for modern OWT designs. Nevertheless, ~~the wind load designs~~ wind loading calculations require the knowledge of turbulence characteristics at heights up to ~~200 m, which was not achieved at SMW nor~~ 250 m, which is not possible at SMW or FINO1. ~~It is therefore,~~ Therefore, it is necessary for future atmospheric measurements to cover this height, where the surface-layer scaling may no longer ~~applicable.~~

be applicable.

Code availability. TEXT

Data availability. TEXT

~~The codes can be made available upon request. The raw data was provided by an external party and therefore cannot be made available.~~

Sample availability. TEXT

Video supplement. TEXT

Appendix A: Sonic anemometer tilt correction

The friction velocity estimates using the double rotation technique, sectoral planar fit and the method by Klipp (2018) are compared in fig. A1. In general, the friction velocity estimates from both methods are in good agreement. The average correlation coefficient for all heights is 0.985 for $|\zeta| \leq 2$. The PF algorithm leads to a slightly larger scatter between u_{*R} and u_*, where the average correlation coefficient from all heights is 0.976 for $|\zeta| \leq 2$ (Table A1). The double rotation algorithm seems to give a smaller deviation between u_{*R} and u_* than the PF algorithm in the present study, which justified the adoption of the double rotation as tilt correction method herein.

Klipp (2018) noted that u_{*R} is appropriate to estimate the friction velocity if the thermal stratification of the atmosphere is neutral only. Yet, fig. A1 suggests that Klipp's method is performing well for non-neutral conditions too, as highlighted by the correlation coefficients in Table A1, which vary between 0.963 to 0.989. Additional studies using measurements from other coastal or offshore sites are needed to assess if such observations are recurring.

Table A1. Correlation coefficients between u_{*R} and u_* using the planar fit (PF) or double rotation (DR)

	$\lvert z/L \rvert \leq 0.1$			$0.1 < \lvert z/L \rvert \leq 2.0$		
	6 m	18 m	45 m	6 m	18 m	45 m
PF	0.989	0.976	0.962	0.981	0.954	0.942
DR	0.995	0.986	0.973	0.989	0.968	0.963

The angle between the stress vector and the wind vector is given as $\alpha = \arctan\left(\overline{v'w'}/\overline{u'w'}\right)$ (Grachev et al., 2003). It is found that α increases from $8°$ at 6 m amsl to $13°$ at 45 m amsl when $\overline{v'w'} < 0$. When $\overline{v'w'} > 0$, α is almost constant

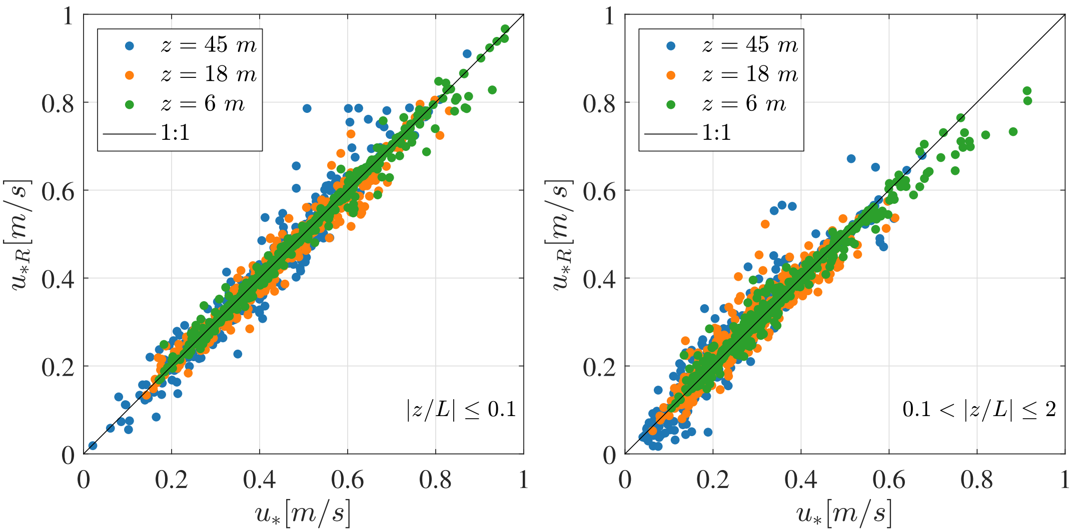

Figure A1. Friction velocity computed using the eddy covariance method with the double rotation method compared with the Klipp method. The left panel considers only $|z/L| \leq 0.1$ and the right panel considers $0.1 < |z/L| \leq 2$.

with the height with an average value of $-7°$. The relatively low value of α, therefore, suggests that the direction of the wind-wave-induced stress is fairly well aligned with the mean wind direction near SMW.

Appendix B: Transducer-shadow effect

The sonic anemometers mounted at 6, 18, and 45 m amsl were omnidirectional solent anemometers, which can be prone to flow distortion by the transducer. Between May 1994 and September 1994, a Gill solent anemometer with an asymmetric head was installed at 10 m amsl on the southern boom of SMW (i.e. on the same side as the other three anemometers). The asymmetric head reduces the flow distortion by the transducer, at least for a specific wind sector. Although the flow distortion by the asymmetric solent was actually unknown, this sensor was used to assess the error on the friction velocity calculated with the omnidirectional solent anemometers. Only wind directions from 220° to 330° were selected, as they corresponded to the sector investigated in the present study.

Flow distortion is assumed to be a function of the angle of attack $\alpha(z)$ and wind direction $\theta(z)$ only. Therefore, using a multivariate regression analysis, it is possible to quantify the variability of $u_*(z)$ with its value at 10 m, denoted $(u_*)_{10}$ as a function of $\alpha(z)$ and $\theta(z)$. For the relatively narrow sector selected, it was found that cubic functions of $\alpha(z)$ and $\theta(z)$ were sufficient to describe this variability. This leads to the following relationship between the friction velocity at 10 m and the one

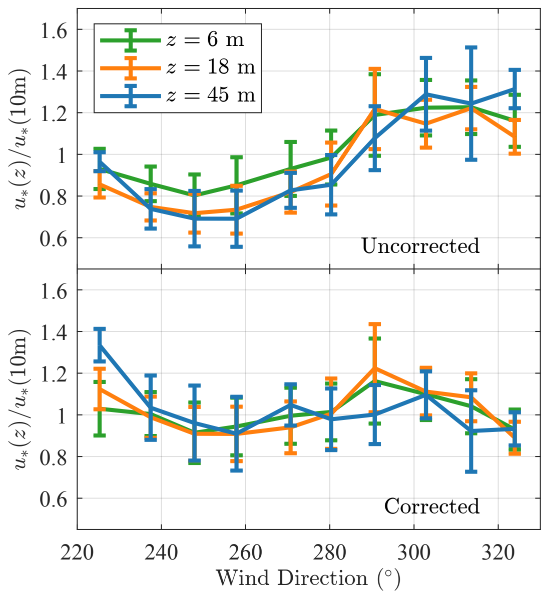

Figure B1. Ratio of the friction velocity by the omnidirectional solent anemometers over the one estimated at 10 m (asymmetric solent anemometer) before (top panel) and after (bottom panel) correction using a multivariate regression analysis. Velocity data recorded between May 1994 and September 1994 for the sector 220°-330° were used (480 samples of 30 min duration) and $|z/L| < 2$ at 10 m amsl.

u_* at a height z:

$$u_*(z) = (u_*)_{10} \cdot \boldsymbol{A}\boldsymbol{X}^\top \tag{B1}$$

$$\boldsymbol{A} = \begin{bmatrix} a_1 & a_2 & a_3 & a_4 & a_5 & a_6 \end{bmatrix} \tag{B2}$$

$$\boldsymbol{X} = \begin{bmatrix} \theta(z) & \theta(z)^2 & \theta(z)^3 & \alpha(z) & \alpha(z)^2 & \alpha(z)^3 \end{bmatrix} \tag{B3}$$

where $\boldsymbol{A}$ is the matrix of coefficients to be determined with the regression analysis. In eq. (B1)-eq. (B3), the friction velocity is not forced to be constant with the height and we do not assume that the flow distortion is similar for the three omnidirectional anemometers.

In the top panel of fig. B1, the maximum variations of the friction velocity between the sonic anemometer at 10 m and 18 m are ±20%. When all the samples in the sector 220°-330° are averaged, the relative difference at 6, 18, and 45 m with respect to the data at 10 m are 4%, 12% and 11%, respectively. After the multivariate regression, the sector-averaged error is nearly zero, although it is clearly not zero for a given wind direction. On average, the friction velocity estimates at 6 m and 10 m are, therefore, almost identical, given that the random error on the friction velocity is above 10% for a sample duration of 30 min (Kaimal and Finnigan, 1994). As shown in fig. B1, the use of sector-averaged flow characteristics may mitigate the influence of transducer-induced flow distortion of the spectral flow characteristics estimated at 6, 18, and 45 m.

A comparison of the power spectral densities of the u-component was conducted with and without the corrected friction velocity. Only data between May 1994 and September 1994 were selected and the Obukhov length was computed at $10\,\mathrm{m}$ amsl. Five stability bins were identified in this data set. However, limited improvement was observed after the application of the correction algorithm. A further comparison was also conducted for the entire dataset, i.e. between May 1994 and July 1995 as shown in fig. B2. This resulted in similar conclusions, where the uncorrected (fig. 10) and the corrected PSDs of the u-component are not too far off. Therefore, it was decided not to use any correction for the friction velocity to avoid over-processing the data.

Author contributions. RMP and EC provided the data curation, formal analysis, methodology, software, and visualization. RMP and EC prepared the original draft. JBJ and CO provided the supervision, review, and editing of the manuscript. All authors contributed to the conceptualization and finalization of the paper.

Competing interests. The authors declare that there ~~are~~ is no conflict of ~~interests~~ interest present.

Disclaimer. TEXT

Acknowledgements. The authors would like to express their gratitude to Dr ~~.~~Kurt Hansen for providing the Vindeby ~~dataset~~data set. Professor Joachim Reuder and Dr ~~.~~Stephan Kral are acknowledged for the fruitful discussion on the wave and wind conditions near SMW.

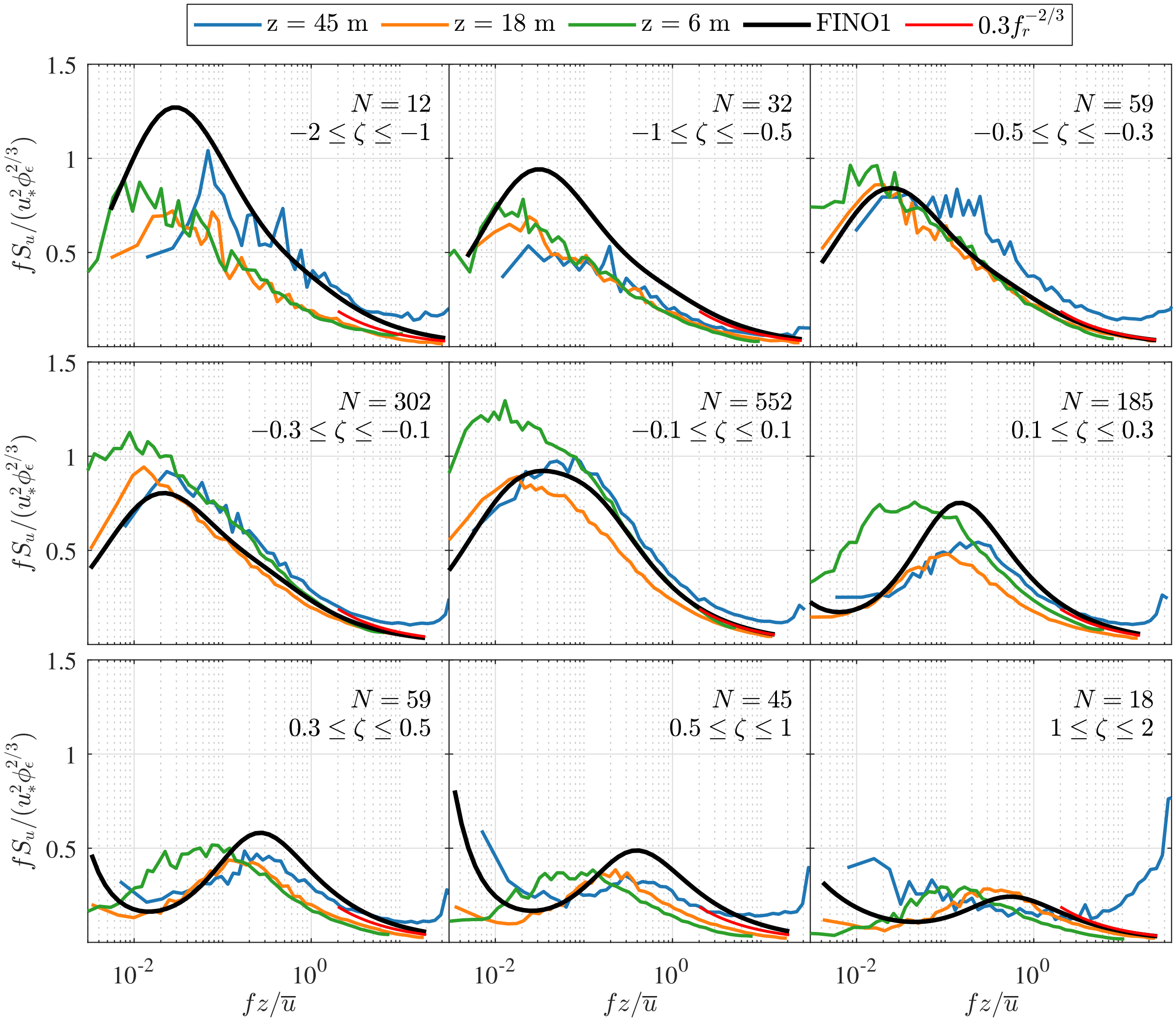

Figure B2. Ratio of the friction velocity by the omnidirectional solent anemometers over the one estimated at 10 m (asymmetric solent anemometer) before (top panel) and after (bottom panel) correction using a multivariate regression analysis. Velocity data recorded between May 1994 and September 1994 for the sector 220°-330° were used (480 samples of 30 min duration) and $|z/L| < 2$ at 10 m amsl.

References

Akaike, H.: Fitting autoregressive models for prediction, Annals of the institute of Statistical Mathematics, 21, 243–247, 1969.

675 Archer, C. L., Colle, B. A., Veron, D. L., Veron, F., and Sienkiewicz, M. J.: On the predominance of unstable atmospheric conditions in the marine boundary layer offshore of the US northeastern coast, Journal of Geophysical Research: Atmospheres, 121, 8869–8885, 2016.

Barthelmie, R. J.: The effects of atmospheric stability on coastal wind climates, Meteorological Applications: A journal of forecasting, practical applications, training techniques and modelling, 6, 39–47, 1999.

Barthelmie, R. J., Courtney, M., Højstrup, J., and Sanderhoff, P.: The Vindeby project: A description, Tech. Rep. 741(EN), Risø National Laboratory, denmark, 1994.

Benasciutti, D. and Tovo, R.: Fatigue life assessment in non-Gaussian random loadings, International journal of fatigue, 28, 733–746, 2006.

Benasciutti, D. and Tovo, R.: Frequency-based fatigue analysis of non-stationary switching random loads, Fatigue & Fracture of Engineering Materials & Structures, 30, 1016–1029, 2007.

Benilov, A. Y., Kouznetsov, O., and Panin, G.: On the analysis of wind wave-induced disturbances in the atmospheric turbulent surface layer, Boundary-Layer Meteorology, 6, 269–285, 1974.

Bowen, A. J., Flay, R. G. J., and Panofsky, H. A.: Vertical coherence and phase delay between wind components in strong winds below 20 m, Boundary-Layer Meteorology, 26, 313–324, 1983.

Chamecki, M. and Dias, N. L.: The local isotropy hypothesis and the turbulent kinetic energy dissipation rate in the atmospheric surface layer, Quarterly Journal of the Royal Meteorological Society: A journal of the atmospheric sciences, applied meteorology and physical oceanography, 130, 2733–2752, 2004.

Cheynet, E.: Influence of the measurement height on the vertical coherence of natural wind, in: Conference of the Italian Association for Wind Engineering, pp. 207–221, 2019.

Cheynet, E., Jakobsen, J. B., Svardal, B., Reuder, J., and Kumer, V.: Wind coherence measurement by a single pulsed Doppler wind lidar, Energy Procedia, 94, 462–477, 2016.

Cheynet, E., Jakobsen, J. B., and Obhrai, C.: Spectral characteristics of surface-layer turbulence in the North Sea, Energy Procedia, 137, 414–427, 2017.

Cheynet, E., Jakobsen, J., and Reuder, J.: Velocity Spectra and Coherence Estimates in the Marine Atmospheric Boundary Layer, Boundary-Layer Meteorology, 169, 429–460, 2018.

Cheynet, E., Jakobsen, J. B., and Snæbjörnsson, J.: Flow distortion recorded by sonic anemometers on a long-span bridge: Towards a better modelling of the dynamic wind load in full-scale, Journal of Sound and Vibration, 450, 214–230, 2019.

Cheynet, E., Flügge, M., Reuder, J., Jakobsen, J. B., Heggelund, Y., Svardal, B., Saavedra Garfias, P., Obhrai, C., Daniotti, N., Berge, J., Duscha, C., Wildmann, N., Husøy Onarheim, I., and Godvik, M.: The COTUR project: Remote sensing of offshore turbulence for wind energy application, Atmospheric Measurement Techniques Discussions, 2021, 1–32, https://doi.org/10.5194/amt-2020-511, 2021.

Chougule, A., Mann, J., Kelly, M., Sun, J., Lenschow, D., and Patton, E.: Vertical cross-spectral phases in neutral atmospheric flow, Journal of Turbulence, p. N36, 2012.

Chougule, A., Mann, J., Kelly, M., and Larsen, G.: *Simplification and Validation of a Spectral-Tensor Model for Turbulence Including Atmospheric Stability*, Boundary-Layer Meteorology, 167, 371–397, 2018.

Davenport, A. G.: The spectrum of horizontal gustiness near the ground in high winds, Quarterly Journal of the Royal Meteorological Society, 87, 194–211, 1961.

De Maré, M. and Mann, J.: Validation of the Mann spectral tensor for offshore wind conditions at different atmospheric stabilities, in: Journal of Physics: Conference Series, vol. 524, p. 012106, IOP Publishing, 2014.

Dobson, F. W.: Review of reference height for and averaging time of surface wind measurements at sea, World Meteorological Organization, 1981.

Doubrawa, P., Churchfield, M. J., Godvik, M., and Sirnivas, S.: Load response of a floating wind turbine to turbulent atmospheric flow, Applied Energy, 242, 1588–1599, 2019.

Drennan, W. M., Kahma, K. K., and Donelan, M. A.: On momentum flux and velocity spectra over waves, Boundary-Layer Meteorology, 92, 489–515, 1999.

Drobinski, P., Carlotti, P., Newsom, R. K., Banta, R. M., Foster, R. C., and Redelsperger, J. L.: The structure of the near-neutral atmospheric surface layer, Journal of the atmospheric sciences, 61, 699–714, 2004.

D'Errico, J.: inpaint_nans (http://kr. mathworks. com/matlabcentral/fileexchange/4551-inpaint-nans), MATLAB Central File Exchange, Retrieved, November, 2021, 2004.

Edson, J. and Fairall, C.: Similarity relationships in the marine atmospheric surface layer for terms in the TKE and scalar variance budgets, Journal of the atmospheric sciences, 55, 2311–2328, 1998.

Emeis, S. and Türk, M.: Wind-driven wave heights in the German Bight, Ocean Dynamics, 59, 463–475, 2009.

ESDU 85020: ESDU 85020Characteristics of atmospheric turbulence near the ground. Part II: single point data for strong winds (neutral atmosphere), 2002.

GE Renewable Energy: Haliade-X offshore wind turbine, https://www.ge.com/renewableenergy/wind-energy/offshore-wind/haliade-x-offshore-turbine, [Online; accessed 08-April-2021], 2021.

Geernaert, G.: Measurements of the angle between the wind vector and wind stress vector in the surface layer over the North Sea, Journal of Geophysical Research: Oceans, 93, 8215–8220, 1988.

Geernaert, G., Hansen, F., Courtney, M., and Herbers, T.: Directional attributes of the ocean surface wind stress vector, Journal of Geophysical Research: Oceans, 98, 16 571–16 582, 1993.

Grachev, A., Fairall, C., Hare, J., Edson, J., and Miller, S.: Wind stress vector over ocean waves, Journal of Physical Oceanography, 33, 2408–2429, 2003.

Grare, L., Lenain, L., and Melville, W. K.: Wave-coherent airflow and critical layers over ocean waves, Journal of Physical Oceanography, 43, 2156–2172, 2013.

Hansen, A. and Butterfield, C.: Aerodynamics of horizontal-axis wind turbines, Annual Review of Fluid Mechanics, 25, 115–149, 1993.

Hansen, K. S., Larsen, G. C., and Ott, S.: Dependence of offshore wind turbine fatigue loads on atmospheric stratification, Journal of Physics: Conference Series, 524, 012 165, 2014.

Högström, U.: Von Karman's constant in atmospheric boundary layer flow: Reevaluated, Journal of atmospheric sciences, 42, 263–270, 1985.

Högström, U.: Non-dimensional wind and temperature profiles in the atmospheric surface layer: A re-evaluation, in: Topics in Micrometeorology. A Festschrift for Arch Dyer, pp. 55–78, Springer, 1988.

Högström, U., Hunt, J., and Smedman, A.-S.: Theory and measurements for turbulence spectra and variances in the atmospheric neutral surface layer, Boundary-Layer Meteorology, 103, 101–124, 2002.

Højstrup, J.: Velocity spectra in the unstable planetary boundary layer, Journal of the Atmospheric Sciences, 39, 2239–2248, 1982.

Hojstrup, J.: A statistical data screening procedure, Measurement Science and Technology, 4, 153, 1993.

Holtslag, M. C., Bierbooms, W. A. A. M., and Van Bussel, G. J. W.: Wind turbine fatigue loads as a function of atmospheric conditions offshore, Wind Energy, 19, 1917–1932, 2016.

Hristov, T., Friehe, C., and Miller, S.: Wave-coherent fields in air flow over ocean waves: Identification of cooperative behavior buried in turbulence, Physical review letters, 81, 5245, 1998.

IEC 61400-1: IEC 61400-3 Wind Turbines Part 1: Design Requirements, 2005.

Jacobsen, A. and Godvik, M.: Influence of wakes and atmospheric stability on the floater responses of the Hywind Scotland wind turbines, Wind Energy, 24, 149–161, 2021.

Janssen, P. A.: Wave-induced stress and the drag of air flow over sea waves, Journal of Physical Oceanography, 19, 745–754, 1989.

Jiang, Q.: Influence of Swell on Marine Surface-Layer Structure, Journal of the Atmospheric Sciences, 77, 1865–1885, 2020.

Jiang, Q., Wang, Q., Wang, S., and Gaberšek, S.: Turbulence adjustment and scaling in an offshore convective internal boundary layer: A CASPER case study, Journal of the Atmospheric Sciences, 77, 1661–1681, 2020.

Johnson, H. K., Højstrup, J., Vested, H. J., and Larsen, S. E.: On the dependence of sea surface roughness on wind waves, Journal of physical oceanography, 28, 1702–1716, 1998.

Jonkman, J. and Musial, W.: Offshore code comparison collaboration (OC3) for IEA Wind Task 23 offshore wind technology and deployment, Tech. rep., National Renewable Energy Lab.(NREL), Golden, CO (United States), 2010.

Kaimal, J. C. and Finnigan, J. J.: Atmospheric Boundary Layer Flows: Their Structure and Measurement, Oxford University Press, 1994.

Kaimal, J. C., Wyngaard, J. C. J., Izumi, Y., and Coté, O. R.: Spectral characteristics of surface-layer turbulence, Quarterly Journal of the Royal Meteorological Society, 98, 563–589, 1972.

Kelly, M.: From standard wind measurements to spectral characterization: turbulence length scale and distribution, Wind Energy Science, 3, 533–543, 2018.

Klipp, C.: Turbulent friction velocity calculated from the Reynolds stress tensor, Journal of the Atmospheric Sciences, 75, 1029–1043, 2018.

Kolmogorov, A. N.: The local structure of turbulence in incompressible viscous fluid for very large Reynolds numbers, Cr Acad. Sci. URSS, 30, 301–305, 1941.

Kondo, J., Fujinawa, Y., and Naito, G.: Wave-induced wind fluctuation over the sea, Journal of Fluid Mechanics, 51, 751–771, 1972.

Kristensen, L. and Jensen, N.: Lateral coherence in isotropic turbulence and in the natural wind, Boundary-Layer Meteorology, 17, 353–373, 1979.

Kristensen, L., Panofsky, H. A., and Smith, S. D.: Lateral coherence of longitudinal wind components in strong winds, Boundary-Layer Meteorology, 21, 199–205, 1981.

Larsén, X. G., Petersen, E. L., and Larsen, S. E.: Variation of boundary-layer wind spectra with height, Quarterly Journal of the Royal Meteorological Society, 144, 2054–2066, 2018.

Leys, C., Ley, C., Klein, O., Bernard, P., and Licata, L.: Detecting outliers: Do not use standard deviation around the mean, use absolute deviation around the median, Journal of Experimental Social Psychology, 49, 764–766, 2013.

Longwet-Higgins, M. S.: On the statistical distribution of the heights of sea waves. J, Journal of Marine Research, 11, 245–266, 1952.

Lumley, J. and Panofsky, H.: The Structure of Atmospheric Turbulence, Interscience monographs and texts in physics and astronomy, Interscience Publishers, 1964.

Mahrt, L., Vickers, D., Howell, J., Højstrup, J., Wilczak, J. M., Edson, J., and Hare, J.: Sea surface drag coefficients in the Risø Air Sea Experiment, Journal of Geophysical Research: Oceans, 101, 14 327–14 335, 1996.

Mahrt, L., Vickers, D., Edson, J., Wilczak, J. M., Hare, J., and Højstrup, J.: Vertical structure of turbulence in offshore flow during RASEX, Journal of Geophysical Research: Oceans, 101, 14 327–14 335, 2001.

Mann, J.: The spatial structure of neutral atmospheric surface-layer turbulence, Journal of fluid mechanics, 273, 141–168, 1994.

Mestayer, P.: Local isotropy and anisotropy in a high-Reynolds-number turbulent boundary layer, Journal of Fluid Mechanics, 125, 475–503, 1982.

Mikkelsen, T., Larsen, S. E., Jørgensen, H. E., Astrup, P., and Larsén, X. G.: Scaling of turbulence spectra measured in strong shear flow near the Earth's surface, Physica Scripta, 92, 124 002, 2017.

Monin, A. S.: The structure of atmospheric turbulence, Theory of Probability & Its Applications, 3, 266–296, 1958.

Monin, A. S. and Obukhov, A. M.: Basic laws of turbulent mixing in the atmosphere near the ground, Tr. Geofiz. Inst., Akad. Nauk SSSR, 24, 163–187, 1954.

Moraes, O. L.: The velocity spectra in the stable atmospheric boundary layer, Boundary-layer meteorology, 43, 223–230, 1988.

Mouzakis, F., Morfiadakis, E., and Dellaportas, P.: Fatigue loading parameter identification of a wind turbine operating in complex terrain, Journal of Wind Engineering and Industrial Aerodynamics, 82, 69–88, 1999.

Naito, G.: Spatial structure of surface wind over the ocean, Journal of Wind Engineering and Industrial Aerodynamics, 13, 67–76, 1983.

Nielsen, F. G., Hanson, T. D., and Skaare, B.: Integrated dynamic analysis of floating offshore wind turbines, in: International Conference on Offshore Mechanics and Arctic Engineering, vol. 47462, pp. 671–679, 2006.

Nieuwstadt, F.: Some aspects of the turbulent stable boundary layer, in: Boundary Layer Structure, pp. 31–55, Springer, 1984.

Nybø, A., Nielsen, F. G., Reuder, J., Churchfield, M. J., and Godvik, M.: Evaluation of different wind fields for the investigation of the dynamic response of offshore wind turbines, Wind Energy, 23, 1810–1830, 2020.

Panofsky, H. and Dutton, J.: Atmospheric Turbulence: Models and Methods for Engineering Applications, A Wiley-interscience publication, Wiley, 1984.

Peña, A. and Gryning, S.-E.: Charnock's roughness length model and non-dimensional wind profiles over the sea, Boundary-layer meteorology, 128, 191–203, 2008.

Peña, A., Dellwik, E., and Mann, J.: A method to assess the accuracy of sonic anemometer measurements, Atmospheric Measurement Techniques, 12, 237–252, 2019.

Power Technology: Full circle: decommissioning the first ever offshore windfarm, https://www.power-technology.com/features/full-circle-decommissioning-first-ever-offshore-windfarm/, [Online; accessed 28-March-2021], 2020.

Putri, R., Obhrai, C., Jakobsen, J., and Ong, M.: Numerical Analysis of the Effect of Offshore Turbulent Wind Inflow on the Response of a Spar Wind Turbine, Energies, 13, 2506, 2020.

Robertson, A., Jonkman, J., Vorpahl, F., Popko, W., Qvist, J., Frøyd, L., Chen, X., Azcona, J., Uzunoglu, E., Guedes Soares, C., et al.: Offshore code comparison collaboration continuation within IEA wind task 30: phase II results regarding a floating semisubmersible wind system, in: International Conference on Offshore Mechanics and Arctic Engineering, vol. 45547, p. V09BT09A012, American Society of Mechanical Engineers, 2014.

Robertson, A. N., Shaler, K., Sethuraman, L., and Jonkman, J.: Sensitivity analysis of the effect of wind characteristics and turbine properties on wind turbine loads, Wind Energy Science, 4, 479–513, 2019.

Rosner, B.: Percentage points for a generalized ESD many-outlier procedure, Technometrics, 25, 165–172, 1983.

Sacré, C. and Delaunay, D.: Structure spatiale de la turbulence au cours de vents forts sur differents sites, Journal of Wind Engineering and Industrial Aerodynamics, 41, 295–303, 1992.

Sanchez Gomez, M. and Lundquist, J. K.: The effect of wind direction shear on turbine performance in a wind farm in central Iowa, Wind Energy Science, 5, 125–139, 2020.

Saranyasoontorn, K., Manuel, L., and Veers, P. S.: A comparison of standard coherence models for inflow turbulence with estimates from field measurements, J. Sol. Energy Eng., 126, 1069–1082, 2004.

Sathe, A. and Bierbooms, W.: Influence of different wind profiles due to varying atmospheric stability on the fatigue life of wind turbines, Journal of Physics: Conference Series, 75, 012 056, 2007.

Sathe, A., Mann, J., Barlas, T., Bierbooms, W., and van Bussel, G.: Influence of atmospheric stability on wind turbine loads, Wind Energy, 16, 1013–1032, 2013.

Schotanus, P., Nieuwstadt, F., and De Bruin, H.: Temperature measurement with a sonic anemometer and its application to heat and moisture fluxes, Boundary-Layer Meteorology, 26, 81–93, 1983.

Sempreviva, A. M. and Gryning, S. E.: Humidity fluctuations in the marine boundary layer measured at a coastal site with an infrared humidity sensor, Boundary-layer meteorology, 77, 331–352, 1996.

Sheinman, Y. and Rosen, A.: A dynamic model of the influence of turbulence on the power output of a wind turbine, Journal of Wind Engineering and Industrial Aerodynamics, 39, 329–341, 1992.

Sjöblom, A. and Smedman, A.-S.: Vertical structure in the marine atmospheric boundary layer and its implication for the inertial dissipation method, Boundary-layer meteorology, 109, 1–25, 2003a.

Sjöblom, A. and Smedman, A.-S.: Vertical structure in the marine atmospheric boundary layer and its implication for the inertial dissipation method, Boundary-layer meteorology, 109, 1–25, 2003b.

Smedman, A. S., Högström, U., and Sjöblom, A.: A note on velocity spectra in the marine boundary layer, Boundary-layer meteorology, 109, 27–48, 2003.

Smedman-Högström, A.-S. and Högström, U.: Spectral gap in surface-layer measurements, Journal of Atmospheric Sciences, 32, 340–350, 1975.

Sorbjan, Z.: On similarity in the atmospheric boundary layer, Boundary-Layer Meteorology, 34, 377–397, 1986.

Soucy, R., Woodward, R., and Panofsky, H.: Vertical cross-spectra of horizontal velocity components at the Boulder observatory, Boundary-Layer Meteorology, 24, 57–66, 1982.

Stiperski, I. and Rotach, M. W.: On the measurement of turbulence over complex mountainous terrain, Boundary-Layer Meteorology, 159, 97–121, 2016.

Stull, R. B.: An Introduction to Boundary Layer Meteorology, Kluwer Academic Publishers, 1 edn., 1988.

Tamura, H., Drennan, W. M., Collins, C. O., and Graber, H. C.: Turbulent airflow and wave-induced stress over the ocean, Boundary-Layer Meteorology, 169, 47–66, 2018.

Taylor, G. I.: The spectrum of turbulence, Proceedings of the Royal Society of London. Series A-Mathematical and Physical Sciences, 164, 476–490, 1938.

Tuomi, L. and Huess, V.: Product user manual for Baltic Sea wave analysis and Forecasting Product, Tech. Rep. CMEMS-BAL-PUM-003-010, Finnish Meteorological Institute, finland, 2020.

Van der Hoven, I.: Power spectrum of horizontal wind speed in the frequency range from 0.0007 to 900 cycles per hour, Journal of Atmospheric Sciences, 14, 160–164, 1957.

Vasiljević, N., Harris, M., Tegtmeier Pedersen, A., Rolighed Thorsen, G., Pitter, M., Harris, J., Bajpai, K., and Courtney, M.: Wind sensing with drone-mounted wind lidars: proof of concept, Atmospheric Measurement Techniques, 13, 521–536, 2020.

Veers, P., Dykes, K., Lantz, E., Barth, S., Bottasso, C. L., Carlson, O., Clifton, A., Green, J., Green, P., Holttinen, H., et al.: Grand challenges in the science of wind energy, Science, 366, 2019.

Vickers, D. and Mahrt, L.: Quality control and flux sampling problems for tower and aircraft data, Journal of atmospheric and oceanic technology, 14, 512–526, 1997.

Vickers, D. and Mahrt, L.: The cospectral gap and turbulent flux calculations, Journal of atmospheric and oceanic technology, 20, 660–672, 2003.

Weber, R. O.: Remarks on the definition and estimation of friction velocity, Boundary-Layer Meteorology, 93, 197–209, 1999.

Weiler, H. S. and Burling, R.: Direct measurements of stress and spectra of turbulence in the boundary layer over the sea, Journal of Atmospheric Sciences, 24, 653–664, 1967.

Welch, P.: The use of fast Fourier transform for the estimation of power spectra: a method based on time averaging over short, modified periodograms, IEEE Transactions on audio and electroacoustics, 15, 70–73, 1967.

Wendell, L., Gower, G., Morris, V., and Tomich, S.: Wind turbulence characterization for wind energy development, Tech. rep., Pacific Northwest Lab., Richland, WA (United States), 1991.

Wetz, T., Wildmann, N., and Beyrich, F.: Distributed wind measurements with multiple quadrotor unmanned aerial vehicles in the atmospheric boundary layer, Atmospheric Measurement Techniques, 14, 3795–3814, 2021.

Wilczak, J., Oncley, S., and Stage, S.: Sonic anemometer tilt correction algorithms, Boundary-Layer Meteorology, 99, 127–150, 2001.

WMO: Guide to meteorological instruments and methods of observation, Secretariat of the World Meteorological Organization, 1983.

Wyngaard, J. and Coté, O.: Cospectral similarity in the atmospheric surface layer, Quarterly Journal of the Royal Meteorological Society, 98, 590–603, 1972.

Wyngaard, J. C.: On the surface-layer turbulence, In D. A. Haugen, Ed., Workshop on Micrometeorology, American Meteorological Society, pp. 101–149, 1973.

Wyngaard, J. C. and Coté, O. R.: The budgets of turbulent kinetic energy and temperature variance in the atmospheric surface layer, Journal of Atmospheric Sciences, 28, 190–201, 1971.